



Probing the $H^\pm W^\mp Z$ interaction at the high energy upgrade of the LHC

Amit Adhikary^{1,a}, Nabarun Chakrabarty^{1,2,b}, Indrani Chakraborty^{2,c}, Jayita Lahiri^{3,4,d}

¹ Centre for High Energy Physics, Indian Institute of Science, C.V.Raman Avenue, Bangalore 560012, India

² Department of Physics, Indian Institute of Technology Kanpur, Kanpur, Uttar Pradesh 208016, India

³ Regional Centre for Accelerator-based Particle Physics, Harish-Chandra Research Institute, HBNI, Chhatnag Road, Jhansi, Allahabad 211019, India

⁴ Department of Physics, Indian Institute of Technology Guwahati, North Guwahati, Assam 781039, India

Received: 11 December 2020 / Accepted: 13 June 2021 / Published online: 28 June 2021

© The Author(s) 2021

Abstract An $H^\pm W^\mp Z$ interaction at the tree level is a common feature of new physics models that feature scalar triplets. In this study, we aim to probe the strength of the aforementioned interaction in a model-agnostic fashion at the futuristic 27 TeV proton-proton collider. We assume that the H^\pm couples dominantly to (W^\pm, Z) and (t, b) and specifically study the processes that involve the $H^\pm W^\mp Z$ vertex at the production level, that is, $pp \rightarrow H^\pm jj$ and $pp \rightarrow ZH^\pm$. Moreover, we look into both $H^\pm \rightarrow W^\pm Z$, tb decays for either production process. Our investigations reveal that the $H^\pm jj$ production process has a greater reach compared to ZH^\pm . Moreover, the discovery potential of a charged Higgs improves markedly with respect to the earlier studies corresponding to lower centre-of-mass energies. Finally, we recast our results in the context of the popular Georgi–Machacek model.

1 Introduction

With the discovery of a Higgs boson of mass 125 GeV [1, 2], the particle spectrum of the Standard Model (SM) is complete. Moreover, the properties of the discovered boson are found to be increasingly consistent with that of the SM Higgs. Despite this success, the SM remains far from being the complete framework. Certain issues on both theoretical and experimental fronts advocate for additional dynamics beyond the SM. Interestingly, extending just the scalar sector of the SM can suffice to address such issues. This puts

forth extended Higgs sectors as prototypes of new physics (NP).

A subset of extended Higgs sectors features additional $SU(2)_L$ scalar multiplets and all of them predict at least one singly charged scalar H^\pm . While the tree level fermionic couplings of H^\pm are generally proportional to the fermion mass for all $SU(2)_L$ representations, it is the coupling to the gauge bosons that can differ. For instance, the $H^\pm W^\mp Z$ interaction vanishes at the tree level for a two-Higgs doublet model (2HDM) [3–6]. This coupling is generated at one-loop [7–10] and hence is generally small in magnitude. And this is true regardless the number of such scalar doublets. On the contrary, the aforementioned coupling is non-zero at the tree level itself in case of $SU(2)_L$ scalar triplets [11–14] and is proportional to the vacuum expectation value (VEV) acquired by the neutral component of the triplet. The triplet VEV is however tightly constrained by measurements of the ρ -parameter for the simplistic Higgs triplet model (HTM) (that employs a complex scalar triplet over and above the doublet) thereby obscuring the observability of the $H^\pm W^\mp Z$ coupling. That said, there exist non-minimal extensions of the HTM where this problem can be circumvented. These involve combining a real scalar triplets with a complex ones in a custodially symmetric manner such that the ρ -parameter is unity for all values of the triplet VEV. The most popular of such extensions arguably is the Georgi–Machacek (GM) model (see [15–34] for a partial list of references) that features an $SU(2)_L \times SU(2)_R$ global symmetry in the scalar potential. This framework predicts two charged Higgses both of which couple to W^\pm, Z . In fact, they also get to interact with the SM fermions by virtue of mixings induced by the scalar potential. Given that the strengths of such Yukawa interactions are proportional to the corresponding fermion masses, the one with the (t, b) pair is of foremost impor-

^a e-mail: amitadhikary@iisc.ac.in

^b e-mails: chakran@iisc.ac.in; nabarunc@iitk.res.in

^c e-mail: indranic@iitk.ac.in (corresponding author)

^d e-mail: jayitalahiri@rind.iitg.ac.in

tance here. The charged Higgses emerging from the more non-minimal extensions also naturally feature sizeable couplings to (W, Z) and (t, b) . Therefore, owing to the fact that the H^+W^-Z interaction features in a plethora of new physics (NP) scenarios, there is the enticing possibility of probing the same in a model-independent fashion.

A singly charged Higgs lighter than the t -quark has been looked for at the LHC via the $t \rightarrow H^+b$ decay. On the other hand, a heavier one is searched in processes where it is produced in association with a t and subsequently decays to a pair of fermions. Such channels include $H^+ \rightarrow t\bar{b}$ [35–37], $H^+ \rightarrow \tau^+\nu_\tau$ [38,39], $H^+ \rightarrow c\bar{b}$ [40] and $H^+ \rightarrow c\bar{s}$ [41]. These searches mainly rely on the strength of the Yukawa interactions of H^+ . In addition, bosonic decays of the form $H^+ \rightarrow W^+X$, where X denotes a scalar have also been of substantial interest [42–45,45–47]. On the other hand, the H^+W^-Z interaction has been probed in $pp \rightarrow H^\pm jj$, $H^\pm \rightarrow W^\pm Z$ [48,49] in context of the GM model and scalar triplet extensions of the minimal supersymmetric standard model (MSSM) [50–53]. A recent review on charged Higgs phenomenology in 2HDM is [54].

In this work, we set out to study the H^+W^-Z interaction at the proposed 27 TeV energy upgrade [55] of the Large Hadron Collider (LHC), the so-called high-energy LHC (HE-LHC). We adopt a generic but simplistic framework comprising H^+W^-Z and H^+tb interactions only. We look for the H^+ in processes that involve the H^+W^-Z coupling at the production vertex. Two such important processes are WZ fusion and the W -mediated $pp \rightarrow ZH^\pm$. Following production, the $H^\pm \rightarrow W^\pm Z$, tb decay modes are looked at and bounds on the corresponding branching fractions are derived corresponding to 15 ab^{-1} integrated luminosity. The generality of the adopted framework makes the obtained results applicable to a wide variety of models that consist of at least one charged Higgs.

The study is organised as follows. We propose the theoretical framework in Sect. 2. The existing LHC constraints and our analysis strategy are discussed in Sect. 3. Section 4 contains the analyses for the proposed channels. The results so obtained are recasted as favoured regions in the model parameter space in Sect. 5. Finally we summarise and conclude in Sect. 6.

2 Theoretical framework

The following Lagrangian describes the dimension ≤ 4 interactions of an H^\pm in a generic fashion [56–58]¹:

$$\mathcal{L} = gM_W F g^{\mu\nu} H^+ W_\mu^- Z_\nu - \frac{\sqrt{2}}{v} H^+ \bar{t} (M_t A_{tb} P_L + M_b B_{tb} P_R) b + \text{h.c.} \quad (1)$$

In the above, F , A_{tb} and B_{tb} are dimensionless parameters quantifying the strengths of the $H^\pm W^\mp Z$ and $H^\pm tb$ interactions respectively. To generate some perspective, we comment here on the typical values for F , A_{tb} and B_{tb} for two specific classes of models. In scalar sectors containing $SU(2)_L$ doublets alone, F is generated radiatively at the one-loop level. The largest $|F|$ for a 2HDM is reported to be $\simeq 0.01$ [59] with further enhancement expected with increasing the number of scalar doublets. For example, addition of an additional *inert* (color-octet) doublet elevates the maximum value of $|F|$ to $\simeq 0.03$ (0.025) [59,60]. While this trend is encouraging, one must note that arbitrarily increasing the number of scalar doublets not only is limited by the experimental constraints such as that of the electroweak T -parameter and the diphoton signal strength, the model becomes aesthetically unattractive and loses predictive power. Therefore, $|F|$ is in the $\mathcal{O}(10^{-2})$ ballpark for realistic multi-doublet extensions of the SM. The other parameter of interest, A_{tb} equals $\cot\beta$ for a 2HDM and its inert doublet and color-octet doublet extensions. Here, $\tan\beta = \frac{v_2}{v_1}$ with v_1 and v_2 denoting the VEVs of the two *active* doublets. Since $\tan\beta < 1$ is ruled out by flavour constraints, one has $A_{tb} < 1$ for a 2HDM. In fact, $\tan\beta \in [1, 10]$ are typical values allowed for the pure 2HDM (see [61] for a global analysis of the 2HDM parameter space) leading to $A_{tb} \in [0.1, 1]$. On the other hand, B_{tb} equals $-\cot\beta$ ($\tan\beta$) for a Type-I (Type-II) 2HDM.

The other class of models are characterised by $SU(2)_L$ scalar triplets where F is non-zero at the tree level itself. One derives $F \simeq \frac{g v_\Delta}{c_W M_W}$ for a single complex triplet. Here, v_Δ , M_W , c_W and g denote the triplet VEV, W -mass, cosine of the Weinberg mixing angle and the $SU(2)_L$ gauge coupling respectively. In this case however, the ρ -parameter constraint dictates $v_\Delta \lesssim 5 \text{ GeV}$ [62] leading to $F \lesssim 0.017$. The singly charged scalar H^+ couples to quarks by virtue of doublet-triplet mixing due to which $A_{tb} = B_{tb} \simeq \frac{2v_\Delta}{v_\phi}$ where v_ϕ denotes the VEV of the SM-like doublet. And the maximum value permitted by the ρ -parameter constraint is $A_{tb} \simeq 0.030$. The small v_Δ for this model therefore renders both $|F|$, $|A_{tb}| \simeq \mathcal{O}(0.01)$. The same is not true in case of the GM model where v_Δ is allowed to be larger by virtue of the global $SU(2)_L \times SU(2)_R$ symmetry of the scalar potential. A global analysis of the minimal GM model in [63] gives the bound $v_\Delta \lesssim 35 \text{ GeV}$ thereby indicating $F \lesssim 0.32$ and $A_{tb} \lesssim 0.56$.

Other possible bosonic and fermionic interactions of H^\pm are not included in the present study. Motivated by the some NP scenarios such as the Type-I 2HDM and the GM model, we further take $M_b B_{tb} \ll M_t A_{tb}$ in this work for the subse-

¹ Momentum dependent interactions borne out of higher dimensional operators [58] have not been considered in this study.

quent analysis. Therefore, with the framework being describable by the two interactions, the total decay width of H^+ reads

$$\Gamma_{H^+} = \Gamma_{H^+ \rightarrow W^+Z} + \Gamma_{H^+ \rightarrow t\bar{b}}. \tag{2}$$

The branching ratios read

$$\text{BR}(H^+ \rightarrow W^+Z) = \frac{\Gamma_{H^+ \rightarrow W^+Z}}{\Gamma_{H^+ \rightarrow W^+Z} + \Gamma_{H^+ \rightarrow t\bar{b}}}, \tag{3a}$$

$$\text{BR}(H^+ \rightarrow t\bar{b}) = \frac{\Gamma_{H^+ \rightarrow t\bar{b}}}{\Gamma_{H^+ \rightarrow W^+Z} + \Gamma_{H^+ \rightarrow t\bar{b}}}. \tag{3b}$$

Finally, we give the expressions for the corresponding partial widths below.

$$\Gamma_{H^+ \rightarrow W^+Z} = \frac{M_{H^+}}{16\pi} \sqrt{\lambda(1, x_W, x_Z)} |F|^2 g^2 \times \left[\frac{(1 - x_W - x_Z)^2}{4x_Z} + 2x_W \right], \tag{4a}$$

$$\Gamma_{H^+ \rightarrow t\bar{b}} = \frac{3g^2 A_{tb}^2 M_t^2 M_{H^+}}{32\pi M_W^2} \sqrt{\lambda(1, x_t, x_b)} (1 - x_t - x_b), \tag{4b}$$

with $\lambda(x, y, z) = x^2 + y^2 + z^2 - 2xy - 2yz - 2zx$. \tag{4c}

Here, $x_P = \frac{M_P^2}{M_{H^+}^2}$ for $P = t, b, W, Z$ and M_{H^+}, M_t, M_b, M_Z are the masses of the charged Higgs, top-quark, bottom-quark and Z-boson respectively. Henceforth, F, A_{tb} and M_{H^+} are counted as the free parameters of the current framework.

3 Analysis strategy and existing LHC limits

Two kinematically distinct topologies for H^\pm production in pp - collisions that involve the $H^\pm W^\mp Z$ interaction are $pp \rightarrow H^\pm jj$ and $pp \rightarrow ZH^\pm$. In the former, an H^\pm is produced by the fusion of W^\pm and Z and two forward jets are emitted. This is essentially vector boson-fusion (VBF) that has close semblance to similar processes for h -production, where, h denotes the SM-like Higgs of mass 125 GeV. On the other hand, the ZH^\pm process is a W -mediated s -channel topology. In this work, we aim to probe the $H^+ \rightarrow W^+Z, t\bar{b}$ decays for both the aforementioned production processes. Leptonic decays of t, W^\pm and Z gives rise to the following four cascades: (a) $pp \rightarrow H^\pm jj \rightarrow W^\pm Zjj \rightarrow 3l + 2j + \cancel{E}_T$, (b) $pp \rightarrow H^\pm jj \rightarrow tbjj \rightarrow 2b + 1l + 2j + \cancel{E}_T$, (c) $pp \rightarrow H^\pm Z \rightarrow W^\pm ZZ \rightarrow 5l + \cancel{E}_T$ and (d) $pp \rightarrow H^\pm Z \rightarrow tbZ \rightarrow 2b + 3l + \cancel{E}_T$, where $l = e, \mu$. The corresponding Feynman diagrams are shown in Fig. 1.

We reiterate for clarity that both processes (a) and (b) describe H^\pm -production via VBF with subsequent decays to $W^\pm Z$ and tb modes respectively. Similarly, processes (c) and

(d) correspond to the $W^\pm Z$ and tb decays of H^\pm produced via $pp \rightarrow ZH^\pm$.

As mentioned before, the framework can be described by M_{H^+} , and the couplings F and A_{tb} . We aim to explore the discovery potential of a 27 TeV pp -machine with integrated luminosity $\mathcal{L} = 15 \text{ ab}^{-1}$ through a detailed signal and background analysis of the aforementioned signal channels. Further, we supplement the conventional cut-based analyses (CBA) with the more sophisticated multivariate analyses (MVA) using the Boosted Decision Tree Decorrelated (BDTD) algorithm [64]. An overview of BDTD analysis will be given in Sect. 4.1.

The performances of the proposed channels can be compared by drawing the exclusion and discovery contours corresponding to each in the $F - A_{tb}$ plane for a given M_{H^+} .

It is imperative to discuss possible exclusions on $\{M_{H^+}, F, A_{tb}\}$ from previous collider searches. The proposed process (a) itself has been searched at the LHC by the ATLAS and CMS collaborations [48, 49]. These searches have placed upper limits on $\sigma_{\text{VBF}} \times \text{BR}(H^+ \rightarrow W^+Z)$ as a function of M_{H^+} . The CMS analysis for $\sqrt{s} = 13 \text{ TeV}$ and integrated luminosity = 15.2 fb^{-1} [49] predicts a stronger bound compared to the one by ATLAS analysis for $\sqrt{s} = 8 \text{ TeV}$ with 20.3 fb^{-1} of integrated luminosity [48] except for $300 \text{ GeV} \leq M_{H^+} \leq 400 \text{ GeV}$. We thus choose to work with the CMS bound in this work. A limit on $\sigma_{\text{VBF}} \times \text{BR}(H^+ \rightarrow W^+Z)$ can be obtained as,

$$|F|^2 \text{BR}(H^+ \rightarrow W^+Z)|_{M_{H^+}} \leq \frac{\left[\sigma_{\text{VBF}} \times \text{BR}(H^+ \rightarrow W^+Z) \right]_{M_{H^+}}^{\text{CMS}}}{\sigma_{|F|=1}|_{M_{H^+}}}. \tag{5}$$

Here $\sigma_{|F|=1}|_{M_{H^+}}$ denotes the $pp \rightarrow H^\pm jj$ cross section in our framework for $|F| = 1$ for a given M_{H^+} in absence of kinematical cuts.

Another pertinent search by ATLAS at 13 TeV and 36.2 fb^{-1} of integrated luminosity is $pp \rightarrow tbH^\pm, H^\pm \rightarrow tb$ [35]. A more stringent bound comes from the recent search at 139 fb^{-1} data [65]. Adopting the more recent bound, a limit on $\sigma_{tbH^\pm} \times \text{BR}(H^+ \rightarrow t\bar{b})$ is derived as :

$$|A_{tb}|^2 \text{BR}(H^+ \rightarrow t\bar{b})|_{M_{H^+}} \leq \frac{\left[\sigma_{tbH^\pm} \times \text{BR}(H^+ \rightarrow t\bar{b}) \right]_{M_{H^+}}^{\text{ATLAS}}}{\sigma'_{|A_{tb}|=1}|_{M_{H^+}}} \tag{6}$$

where, $\sigma'_{|A_{tb}|=1}|_{M_{H^+}}$ denotes the $pp \rightarrow tbH^\pm$ cross section for $|A_{tb}| = 1$ for a given M_{H^+} in absence of kinematical cuts.

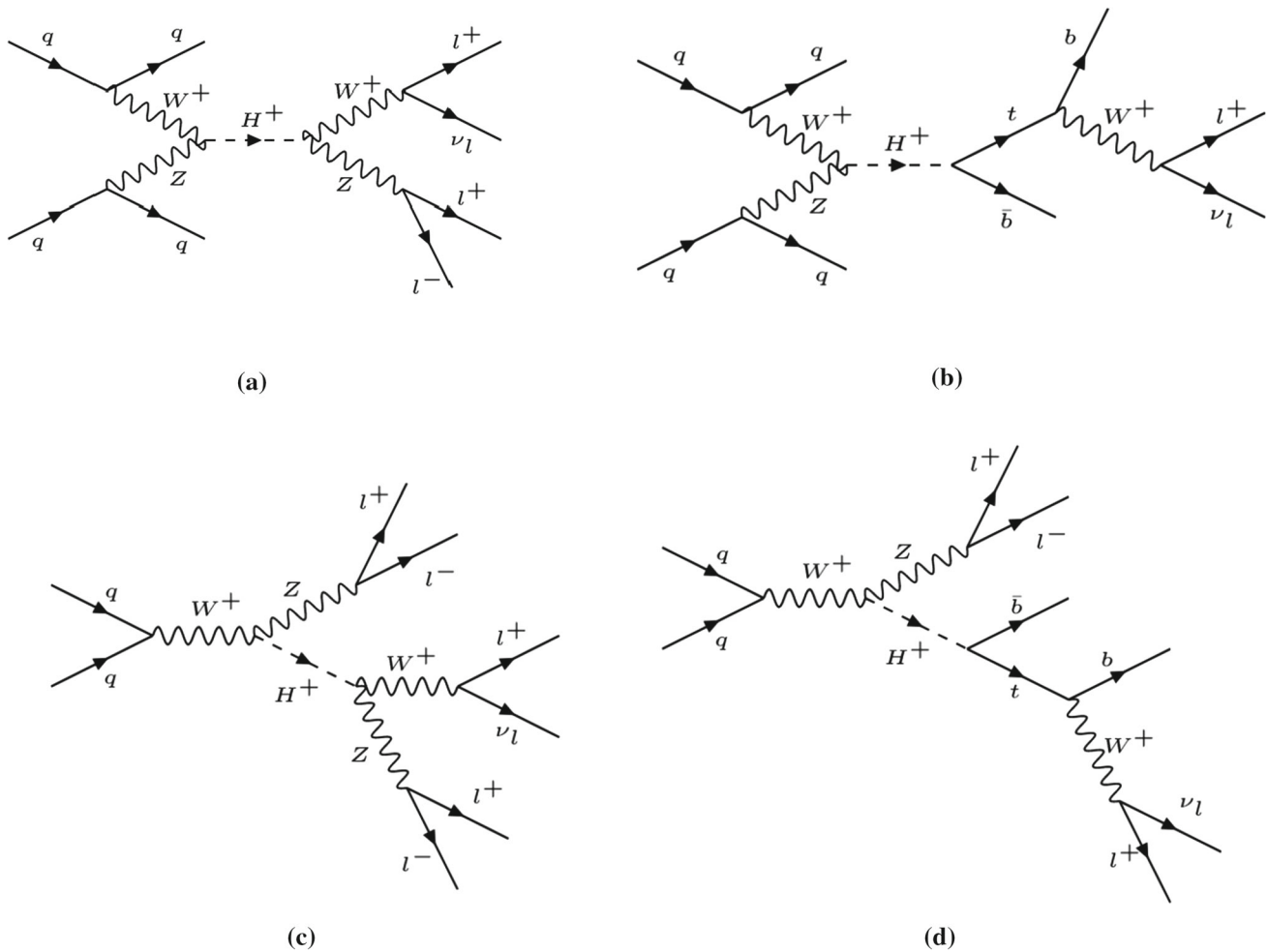


Fig. 1 Feynman diagrams representing the processes (a) $pp \rightarrow H^\pm jj \rightarrow W^\pm Z jj \rightarrow 3l + 2j + \cancel{E}_T$, (b) $pp \rightarrow H^\pm jj \rightarrow tbjj \rightarrow 2b + 1l + 2j + \cancel{E}_T$, (c) $pp \rightarrow H^\pm Z \rightarrow W^\pm ZZ \rightarrow 5l + \cancel{E}_T$ and (d) $pp \rightarrow H^\pm Z \rightarrow tbZ \rightarrow 3l + 2b + \cancel{E}_T$. In the diagram, j represents the a light quark jet, while l^\pm denote e, μ

4 Collider analysis

We choose to perform analyses for $M_{H^+} = 200$ GeV, 300 GeV, 500 GeV and 1 TeV which we tag as BP1, BP2, BP3 and BP4 respectively. The signal and background samples are generated using MG5aMC@NLO [66] at the leading order (LO). The NN23LO1 Parton Distribution Function (PDF) set and default hadronization and factorization scales are used. The parton level events are passed on to pythia8 [67] for showering and hadronisation and subsequently to Delphes-3.4.1 for detector simulation. Specifically, we have throughout used the default ATLAS detector simulation card that comes with Delphes-3.4.1 [68]. The multivariate analysis is done using the TMVA package [69]. The signal significance S is derived using $S = \sqrt{2 \left[(N_S + N_B) \log \left(\frac{N_S + N_B}{N_B} \right) - N_S \right]}$

[70], with $N_S(N_B)$ denoting the number of signal (background) events surviving the kinematical cuts.²

In order to estimate the effects on the final signal significance by assuming a systematic uncertainty of σ_{sys_un} , the signal significance formula changes as:

² The number of signal (N_S) and the background (N_B) events can be calculated as:

$$N_{S(B)} = \sigma_{S(B)} \times \mathcal{L} \times \epsilon_{S(B)}, \quad (7)$$

where $\sigma_{S(B)}$, \mathcal{L} , $\epsilon_{S(B)}$ denote the signal (background) cross section, integrated luminosity and signal (background) cut-efficiency respectively.

Table 1 The LO cross sections for signal and backgrounds for the process $pp \rightarrow H^\pm jj \rightarrow W^\pm Zjj \rightarrow 3l + 2j + \cancel{E}_T$. The signal cross sections are computed for the $(F, BR(H^+ \rightarrow W^+Z)) = (0.4, 0.4)$ reference point

Signal/backgrounds	Process	Cross section σ (LO) (fb)
Signal		
BP1 ($M_{H^+} = 200$ GeV)		5.49
BP2 ($M_{H^+} = 300$ GeV)	$pp \rightarrow H^\pm jj \rightarrow W^\pm Zjj \rightarrow 3l + 2j + \cancel{E}_T$	3.43
BP3 ($M_{H^+} = 500$ GeV)		1.64
BP4 ($M_{H^+} = 1$ TeV)		0.46
Backgrounds		
	$pp \rightarrow W^\pm Zjj \rightarrow 3l + 2j + \cancel{E}_T$	120.0
	$pp \rightarrow ZZjj \rightarrow 4l + 2j$	4.57
	$pp \rightarrow W^\pm ZZ \rightarrow 3l + 2j + \cancel{E}_T$	1.19
	$pp \rightarrow W^\pm W^\mp Z \rightarrow 3l + 2j + \cancel{E}_T$	4.80
	$pp \rightarrow t\bar{t}Z \rightarrow 4l + 2b + \cancel{E}_T$	10.15
	$pp \rightarrow t\bar{t}W^\pm \rightarrow 3l + 2b + \cancel{E}_T$	11.50
	$pp \rightarrow ZZZ \rightarrow 4l + 2j$	8.25×10^{-3}
	$pp \rightarrow W^\pm ZZ \rightarrow 4l + 2j$	8.75×10^{-2}

$$S_{\text{sys}} = \sqrt{2 \left((N_S + N_B) \log \left(\frac{(N_S + N_B)(N_B + \sigma_B^2)}{N_B^2 + (N_S + N_B)\sigma_B^2} \right) - \frac{N_B^2}{\sigma_B^2} \log \left(1 + \frac{\sigma_B^2 N_S}{N_B(N_B + \sigma_B^2)} \right) \right)}, \tag{8}$$

where $\sigma_B = \sigma_{\text{sys}_{un}} \times B$.

We set out to analyse the various channels following the aforementioned strategy. For processes (a), (c) and (b), (d) in Fig. 1, $(F, BR(H^+ \rightarrow W^+Z))$ and $(F, BR(H^+ \rightarrow t\bar{b}))$ are respectively treated as the free parameters. That said, for a given signal, it is important to compare the results from CBA to those from MVA for specific reference values of F and the branching ratios. Therefore, we take $(F, BR(H^+ \rightarrow W^+Z)) = (0.4, 0.4)$ and $(F, BR(H^+ \rightarrow t\bar{b})) = (0.4, 0.4)$ as the reference for processes (a), (c) and (b), (d) respectively for the ensuing analysis.

4.1 The $3l + 2j + \cancel{E}_T$ channel

This subsection discusses the VBF production of H^\pm followed by the $H^\pm \rightarrow W^\pm Z$ decay. The VBF topology always leads to a couple of light jets in the forward and backward directions with negligible hadronic activity in the intervening rapidity gap. Since the two jets (j_1, j_2) reside in different η -hemisphere for VBF production, the forward (backward) jet is identified by $\eta > 0$ ($\eta < 0$). We therefore demand $\eta_{j_1}\eta_{j_2} < 0$ to tag the two leading light jets as forward and backward ones. The $H^\pm \rightarrow W^\pm Z$ decay ultimately leads to three leptons, two of which are of same flavor and opposite sign (SFOS) that come from Z and the third one comes from W^\pm . In addition, a neutrino also originates from W^\pm . We choose to treat the $H^\pm \rightarrow W^\pm Z$ branching ratio as a free parameter at this level. The signal cross sections for different M_{H^+} are given in Table 1.

The most dominant SM backgrounds corresponding to signal come from $W^\pm Zjj$ and $ZZjj$ production followed by leptonic cascades. These two background processes involve jets at the production level as does the signal. Therefore, we demanded $p_T^j > 20$ GeV, $M_{j_1 j_2} > 500$ GeV, $|\eta_j| < 5$ while generating these in order to pick out the phase space kinematically relevant to the VBF topology. The resulting LO cross sections of these two background processes along with their leptonic decay chains are given in Table 1. Sub-leading contributions to the backgrounds come from W^+W^-Z , $W^\pm ZZ$, ZZZ , $t\bar{t}W^\pm$, $t\bar{t}Z$. We do not impose cuts at the generation level for the sub-leading ones since they do not involve jets at the production level, and, the corresponding cross sections are again listed in Table 1. A couple of observations then emerge. First, $W^\pm ZZ \rightarrow 4l + 2j$, ZZZ have negligible cross sections compared to the leading backgrounds. Secondly, though it might naively appear that the other sub-leading channels offer rates comparable to, or, even higher than $ZZjj$, one must remember that their cross sections are computed in the absence of kinematical cuts. Therefore, stringent VBF selection cuts almost nearly obliterate $t\bar{t}W^\pm$, $t\bar{t}Z$, $W^\pm ZZ \rightarrow 3l + 2j + \cancel{E}_T$. In all, it is only the $W^\pm Zjj$ and $ZZjj$ channels that are kinematically relevant to the analysis.

Events are selected by demanding at least two light jets ($N_j \geq 2$) and three leptons after vetoing b -jets and τ -jets in the final state. Of the two hardest light jets, one is demanded to be forward and the other as the backward one as mentioned earlier. We first initiate the cut-based approach. The following

Table 2 The optimised selection cuts for the $3l + 2j + \cancel{E}_T$ channel for the four benchmarks

M_{H^+}	A_1	A_2	A_3	A_4
200 GeV	$M_{j_1 j_2} > 500$ GeV	$ \Delta\eta_{j_1 j_2} > 5$	$ M_{\text{inv}}^{WZ} - M_{H^+} < 50$ GeV	$ M_T^{WZ} - M_{H^+} < 100$ GeV
300 GeV	$M_{j_1 j_2} > 500$ GeV	$ \Delta\eta_{j_1 j_2} > 5.5$	$ M_{\text{inv}}^{WZ} - M_{H^+} < 50$ GeV	$ M_T^{WZ} - M_{H^+} < 50$ GeV
500 GeV	$M_{j_1 j_2} > 500$ GeV	$ \Delta\eta_{j_1 j_2} > 6$	$ M_{\text{inv}}^{WZ} - M_{H^+} < 60$ GeV	$ M_T^{WZ} - M_{H^+} < 125$ GeV
1 TeV	$M_{j_1 j_2} > 500$ GeV	$ \Delta\eta_{j_1 j_2} > 4.5$	$ M_{\text{inv}}^{WZ} - M_{H^+} < 60$ GeV	$ M_T^{WZ} - M_{H^+} < 120$ GeV

trigger-level cuts are applied:

$$p_T^l > 10 \text{ GeV}, |\eta_{j,l}| < 2.5, \Delta R_{l_1 l_2} > 0.2, \Delta R_{jl} > 0.2, \Delta R_{j_1 j_2} > 0.4. \tag{9}$$

To start with, we shall compute the signal significance using the cut-based method. In addition to the trigger cuts, certain specific kinematic variables are identified to extract the signal with higher efficiency. They are $M_{j_1 j_2}, |\Delta\eta_{j_1 j_2}|, M_{\text{inv}}^{WZ}, M_T^{WZ}$. We denote the corresponding cuts to be A_1, A_2, A_3, A_4 respectively and they are optimised by looping over a few configurations and selecting the one that yields the maximum statistical significance. The cut-flow for the signal and background processes corresponding to the chosen BPs are displayed in Tables 3, 4, 5 and 6. The following discussion motivates these variables and compares the signal and backgrounds in their terms.

- A_1 and A_2 : A VBF topology demands a high invariant mass of the two forward jet system ($M_{j_1 j_2}$) and a large separation between their pseudo rapidities ($|\Delta\eta_{j_1 j_2}|$). Thus high invariant mass cuts (given in Table 2) are used for all the benchmarks. Strong cuts on $|\Delta\eta_{j_1 j_2}|$ for enhancing the significance for all benchmark points can be found in Table 2. Corresponding normalised distributions for both signal and backgrounds are drawn in Fig. 2(d), (e). It can be observed that the peak of $M_{j_1 j_2}$ distribution shifts towards higher value with increase in M_{H^+} . From the distributions, it is evident that these cuts reduce the backgrounds to a large extent. The same is also reflected in the first two columns of Tables 3, 4 and 5.
- A_3 : Next comes a cut on the invariant mass of the $3l + \cancel{E}_T$ system (M_{inv}^{WZ}), which must peak at the mass of the decaying H^+ in case of the signal. For constructing this variable, we have taken into account two possible combinations comprising of one same flavour opposite sign (SFOS) lepton pair (peaking at M_Z), one isolated lepton coming from W -boson and z -component of missing transverse energy.³ Two solutions of the z -component of

³ $\cancel{E}_{T,z} = \frac{1}{2p_T^l} (A_W p_z^l \pm E^l \sqrt{A_W^2 - 4p_T^{l2} \cancel{E}_T^2})$, where $A_W = M_W^2 + 2(p_x^l \cancel{E}_{T,x} + p_y^l \cancel{E}_{T,y})$. $\cancel{E}_{T,x}$ and $\cancel{E}_{T,y}$ are the x and y component of the missing transverse momentum.

missing transverse energy lead to two different kinematic variables : $(M_{\text{inv}}^{WZ})_1$ and $(M_{\text{inv}}^{WZ})_2$. Comparing these two variables with M_{H^+} , the closest one is chosen to be M_{inv}^{WZ} . For clarity we have plotted distributions of $(M_{\text{inv}}^{WZ})_1$ and $(M_{\text{inv}}^{WZ})_2$ for both signal and dominant backgrounds before applying any cut. Whereas, for backgrounds since the source of $3l + \cancel{E}_T$ is not a single particle, the corresponding distributions of $(M_{\text{inv}}^{WZ})_1$ and $(M_{\text{inv}}^{WZ})_2$ in Fig. 2(a), (b) do not peak around M_{H^+} .⁴

- A_4 : Another potentially important variable for this signal is the transverse mass of WZ -system. It can be constructed as:

$$M_T^{WZ} = \sqrt{[E_T(W) + E_T(Z)]^2 - [\vec{p}_T(W) + \vec{p}_T(Z)]^2} \tag{10}$$

where $\vec{p}_T(W)$ is computed by adding \vec{p}_T^{miss} and \vec{p}_T of the lepton (coming from W^\pm) vectorially and $E_T(W)$ is obtained from the scalar sum of p_T^{miss} and the lepton transverse energy. $\vec{p}_T(Z)$ is constructed by adding the \vec{p}_T of the two leptons of SFOS that peak near the Z -mass and $E_T(Z)$ is calculated using the following relation.

$$E_T^2(Z) = |\vec{p}_T(Z)|^2 + M_Z^2 \tag{11}$$

As the W^\pm, Z coming from heavy H^\pm are highly boosted, peak of the normalised distribution of M_T^{WZ} will be shifted to the higher end starting from BP1 to BP4 in Fig. 2(c). The optimised set of cuts on M_T^{WZ} can be found in Table 2.

Overall, the CBA shows that $M_{H^+} = 500$ GeV has the highest observability. Next we perform an MVA to improve over the results obtained from cut-based analysis. Before going to perform the MVA analysis, let us elaborate on the details of the same. Here the MVA is performed using *decorrelated boosted decision tree* (BDTD) algorithm within the toolkit for multivariate data analysis (TMVA) framework.

First the signal and the background-like events are distinguished using *decision trees* as classifier. To segregate the

⁴ While drawing the distributions, we only have shown the distribution for two dominant backgrounds, i.e. $W^\pm Zjj$ and $ZZjj$.

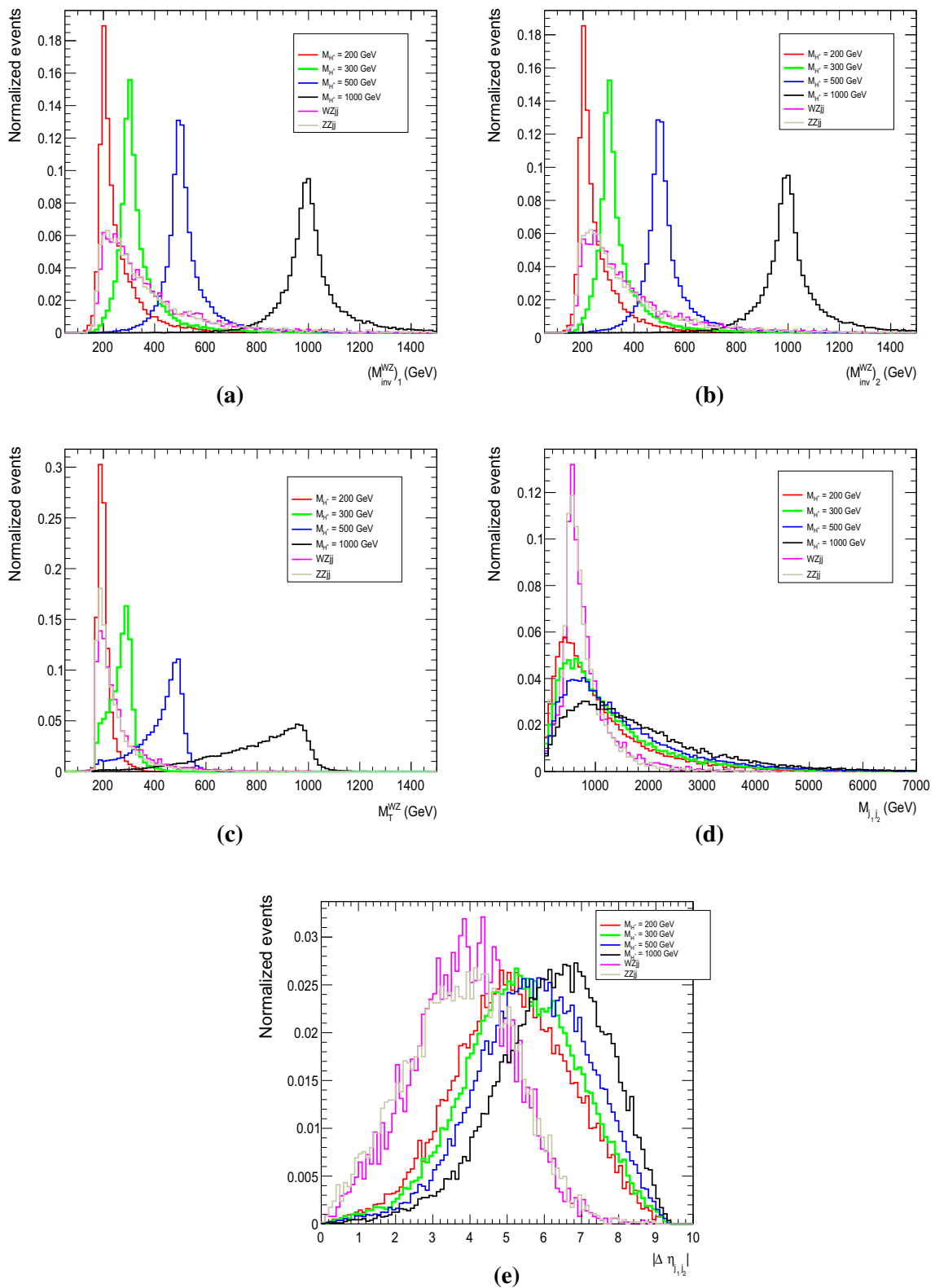


Fig. 2 Normalised distributions of $(M_{inv}^{WZ})_1$, $(M_{inv}^{WZ})_2$, M_T^{WZ} , $M_{j_1j_2}$ and $|\Delta\eta_{j_1j_2}|$ for the $3l + 2j + \cancel{E}_T$ channel

Table 3 Signal and background yields after applying the selection cuts and projected signal significance for BP1 with 15 ab^{-1} integrated luminosity. The signal yields are computed for the $(F, \text{BR}(H^+ \rightarrow W^+Z)) = (0.4, 0.4)$ reference point

$M_{H^+} = 200 \text{ GeV}$	NEV ($\mathcal{L} = 15 \text{ ab}^{-1}$)			
	A_1	A_2	A_3	A_4
Signal	7170	3916	3190	3183
$W^\pm Zjj$	88484	11462	4662	4647
$ZZjj$	4637	622	301	301
Signal yield = 3138	Total background yield = 4948		Signal significance (0% $\sigma_{\text{sys_un}}$) = 40.8 Signal significance (2% (5%) $\sigma_{\text{sys_un}}$) = 22.3 (10.3)	

Table 4 Signal and background yields after applying the selection cuts and projected signal significance for BP2 with 15 ab^{-1} integrated luminosity. The signal yields are computed for the $(F, \text{BR}(H^+ \rightarrow W^+Z)) = (0.4, 0.4)$ reference point

$M_{H^+} = 300 \text{ GeV}$	NEV ($\mathcal{L} = 15 \text{ ab}^{-1}$)			
	A_1	A_2	A_3	A_4
Signal	5529	2433	2057	1591
$W^\pm Zjj$	89118	6300	2934	1494
$ZZjj$	4599	316	135	68
Signal yield = 1591	Total background yield = 1562		Signal significance (0% $\sigma_{\text{sys_un}}$) = 35.3 Signal significance (2% (5%) $\sigma_{\text{sys_un}}$) = 26.3 (14.5)	

Table 5 Signal and background yields after applying the selection cuts and projected signal significance for BP3 with 15 ab^{-1} integrated luminosity. The signal yields are computed for the $(F, \text{BR}(H^+ \rightarrow W^+Z)) = (0.4, 0.4)$ reference point

$M_{H^+} = 500 \text{ GeV}$	NEV ($\mathcal{L} = 15 \text{ ab}^{-1}$)			
	A_1	A_2	A_3	A_4
Signal	3283	1254	1050	942
$W^\pm Zjj$	88484	2912	489	172
$ZZjj$	4637	157	26	6
Signal yield = 942	Total background yield = 178		Signal significance (0% $\sigma_{\text{sys_un}}$) = 47.3 Signal significance (2% (5%) $\sigma_{\text{sys_un}}$) = 44.0 (34.4)	

Table 6 Signal and background yields after applying the selection cuts and projected signal significance for BP4 with 15 ab^{-1} integrated luminosity. The signal yields are computed for the $(F, \text{BR}(H^+ \rightarrow W^+Z)) = (0.4, 0.4)$ reference point

$M_{H^+} = 1 \text{ TeV}$	NEV ($\mathcal{L} = 15 \text{ ab}^{-1}$)			
	A_1	A_2	A_3	A_4
Signal	862	654	491	262
$W^\pm Zjj$	88484	19602	324	15
$ZZjj$	4637	1065	178	0
Signal yield = 262	Total background yield = 15		Signal significance (0% $\sigma_{\text{sys_un}}$) = 33.0 Signal significance (2% (5%) $\sigma_{\text{sys_un}}$) = 32.6 (31.0)	

signal and background-like events depending on its *purity*,⁵ each node of the decision tree is associated with one discerning variable on which an optimised cut value is imposed. By modifying the BDTD variable nCuts, one can perform the aforementioned task within TMVA. Starting from the zeroth

⁵ The purity p can be defined as: $p = \frac{S}{S+B}$. An event can be tagged as signal (background) when $p > 0.5$ ($p < 0.5$).

node or root node, the training of the decision trees is carried on unless a particular depth (MaxDepth) specified by the user is achieved. Finally from the final *leaf nodes*, an event can be tagged as signal or background according to the purity.

The decision trees being prone to statistical fluctuations of the training sample, are said to be weak classifiers. This problem can be alleviated by combining a set of weak clas-

sifiers into a stronger one through the modification of the weight of the events. One can thus create new decision trees using this particular procedure termed as *Boosting*. Throughout the analysis, we have used *Adaptive boost*, compatible for weak classifiers, with input variable transforming in a decorrelated manner. Within TMVA framework, it can be realised as Decorrelated AdaBoost. The BDTD parameters like the number of decision trees N_{Trees} , the maximum depth of the decision tree allowed $MaxDepth$, the minimum percentage of training events in each leaf node $MinNodeSize$ and $NCuts$ for four benchmarks of our analysis have been tabulated in Table 7. To get rid of the overtraining of the signal and background samples, the results of the Kolmogorov–Smirnov test, *i.e.* Kolmogorov–Smirnov score (KS-score) should be > 0.1 as well as stable. In fact, KS-score > 0.01 can also avoid the overtraining if it remains stable even after changing the internal parameters of the algorithm. Now the BDTD algorithm makes a ranking list out of the kinematic variables that are fed into the algorithm, according to the performance of variables in separating signal from backgrounds. Several kinematic variables might be highly correlated. We select a reasonable number of top ranking variables among them for providing best possible separation between the signal and backgrounds. Thus for this channel following kinematic variables with maximum discerning abilities are proposed for MVA:

$$\eta_{j_1}, \eta_{j_2}, \Delta R_{j_1 j_2}, p_T^{l_1}, p_T^{l_3}, \Delta R_{l_1 j_1}, \Delta R_{l_2 j_1}, \Delta R_{l_1 j_2}, \Delta R_{l_2 j_2}, p_T^{j_1 j_2}, p_T^{l_1 l_2 l_3}, M_{j_1 j_2}, M_{j_1 j_2 l_1 l_2 l_3}, \cancel{E}_T, M_{inv}^{WZ}, p_{T,vec}^{tot}, M_T^{WZ} \tag{12}$$

Here, ΔR_{ij} denotes the distance in the $\eta - \phi$ plane between the i th and j th particle. While p_T^{ijk} ($p_{T,vec}^{ijk}$) is the scalar (vector) sum of the transverse momentum of the system of i th, j th and k th particle, $M_{j_1 j_2 l_1 l_2 l_3}$ represents invariant mass of “ j_1, j_2, l_1, l_2, l_3 ”-system. The rest of the variables have been defined earlier in the text. According to the BDT ranking, among these variables, the five most important variables to differentiate the signal from backgrounds are : $p_T^{j_1 j_2}, M_{inv}^{WZ}, M_{j_1 j_2 l_1 l_2 l_3}, M_{j_1 j_2}, M_T^{WZ}$.

Figure 18(a)–(d) in Appendix A depict the KS-scores for signal and backgrounds for all four benchmarks. KS-scores have also been tabulated in Table 7 for convenience. To maximise the significance, one can adjust *BDT cut value* or *BDT score*. The BDT cut values adjusted for four benchmarks can be found in Table 7. In Fig. 3(a), we have presented the variation of the signal significances with BDT score. Here it can be easily inferred that the significance attains a maximum value at a particular BDT score.⁶ Next we draw Receiver’s Opera-

tive Characteristic (ROC) curves⁷ for all benchmarks in Fig. 3(b), to estimate the degree of rejecting the backgrounds with respect to the signal. From Fig.3, it can be inferred that the degree of rejecting backgrounds reduces with decrease in M_{H^+} . But owing to large signal cross section of BP1 compared to the rest of the three BPs, BP1 fares the best in probing this channel.

The yields for signal (for $M_{H^+} = 200$ GeV, 300 GeV, 500 GeV, 1 TeV) and corresponding backgrounds after optimisation through BDTD-analysis are given in Table 8. The numbers events are computed taking $F = 0.4$ and $BR(H^+ \rightarrow W^+Z) = 40\%$ at $\mathcal{L} = 15 \text{ ab}^{-1}$. BP1 is seen to offer the highest observability through MVA. And this observability decreases upon increasing M_{H^+} . Importantly, the MVA is seen to yield higher statistical significance than the CBA for all the values of M_{H^+} . The maximum improvement of significance (with respect to the cut-based analysis) is $\simeq 35\%$ which occurs for $M_{H^+} = 300$ GeV. Besides, we have computed the significances taking into account 2% and 5% systematic uncertainties in Table 8.

We remark here that N_S for each BP can be extrapolated for arbitrary F and $BR(H^+ \rightarrow W^+Z)$ by appropriately scaling the number corresponding to the $(F, BR(H^+ \rightarrow W^+Z)) = (0.4, 0.4)$ reference point. Given the MVA outperforms the CBA for all the BPs, the numbers from the former scaled to draw contours in the $BR(H^+ \rightarrow W^+Z)$ vs $|F|$ plane as shown in Fig. 4.

4.2 The $2b + 1l + 2j + \cancel{E}_T$ channel

In the previous subsection we explored VBF production of the charged Higgs H^\pm where one forward and one backward light jet is produced along with H^\pm and H^\pm further decays into W^\pm and Z . In this subsection, the $H^\pm \rightarrow tb$ decay is probed with the t decaying leptonically leading to a final state containing two b -tagged jets, two light jets, one isolated lepton (leptons include electron, muon) and \cancel{E}_T . Forward and backward jet-tagging has been done using the criteria mentioned earlier. Here, the dominant background contribution comes from top pair production. There are two possibilities, *viz.* semi-leptonic decay of $t\bar{t}$, where one of the top quarks decays hadronically or full leptonic decay of $t\bar{t}$, where both the top quarks decay leptonically. The next dominant contribution comes from QCD-QED $2bl\nu jj$ ($l = e, \mu$) production. We also generate the subdominant backgrounds, *viz.* $t\bar{t}h, t\bar{t}Z, t\bar{t}W$ and W -boson associated single top production or tW . Among these the tW background is generated with one extra parton in the final state and here the W -bosons are decayed in all possible channels which can give rise to the final state of our interest. The cross sections for the cho-

⁶ If the curves show any fluctuations, then we put the BDT cut value just before the curve starts fluctuating.

⁷ ROC curve is a plot of signal efficiency (ϵ_S) vs. efficiency of rejecting the backgrounds ($1 - \epsilon_B$), ϵ_B being the background efficiency.

Table 7 Tuned BDT parameters for BP1, BP2, BP3 and BP4 for the $3l + 2j + \cancel{E}_T$ channel

	NTrees	MinNodeSize	MaxDepth	nCuts	KS-score for signal (background)	BDT Score
BP1	180	3 %	2.0	35	0.251 (0.621)	0.02
BP2	100	4 %	2.0	60	0.409 (0.524)	0.148
BP3	150	3 %	2.0	39	0.11 (0.541)	0.232
BP4	200	3 %	2.0	35	0.346 (0.054)	0.19

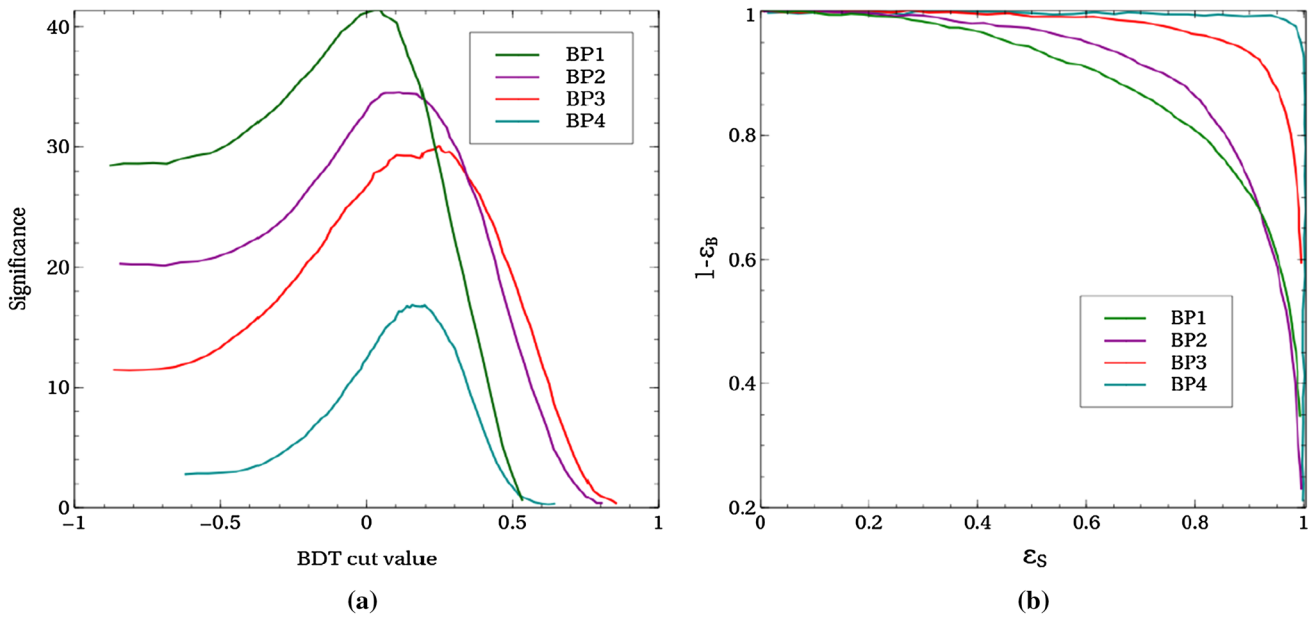


Fig. 3 (a) Variation of significance with BDT-score for $3l + 2j + \cancel{E}_T$ channel. (b) ROC curves for chosen benchmark points for $3l + 2j + \cancel{E}_T$ channel

Table 8 The signal and background yields at 15 ab^{-1} for $M_{H^+} = 200 \text{ GeV}$, 300 GeV , 500 GeV and 1 TeV along with signal significances for the $3l + 2j + \cancel{E}_T$ channel after the BDTD analysis. The signal yields are computed for the $(F, \text{BR}(H^+ \rightarrow W^+ Z)) = (0.4, 0.4)$ reference point

$M_{H^+} = 200 \text{ GeV}$			$M_{H^+} = 300 \text{ GeV}$		
Process	Yield at 15 ab^{-1}		Process	Yield at 15 ab^{-1}	
Background	$W^\pm Zjj$	3502	Background	$W^\pm Zjj$	1119
	$ZZjj$	130		$ZZjj$	33
	Total	3632		Total	1152
Signal ($pp \rightarrow H^\pm jj \rightarrow 3l + 2j + \cancel{E}_T$)		3506	Signal ($pp \rightarrow H^\pm jj \rightarrow 3l + 2j + \cancel{E}_T$)		1955
Significance ($0\% \sigma_{\text{sys_un}}$)		51.3	Significance ($0\% \sigma_{\text{sys_un}}$)		47.5
Signal significance ($2\% (5\%) \sigma_{\text{sys_un}}$)		30.5 (14.6)	Signal significance ($2\% (5\%) \sigma_{\text{sys_un}}$)		36.8 (21.2)
$M_{H^+} = 500 \text{ GeV}$			$M_{H^+} = 1 \text{ TeV}$		
Process	Yield at 15 ab^{-1}		Process	Yield at 15 ab^{-1}	
Background	$W^\pm Zjj$	320	Background	$W^\pm Zjj$	14
	$ZZjj$	9		$ZZjj$	1
	Total	329		Total	15
Signal ($pp \rightarrow H^\pm jj \rightarrow 3l + 2j + \cancel{E}_T$)		1179	Signal ($pp \rightarrow H^\pm jj \rightarrow 3l + 2j + \cancel{E}_T$)		311
Significance ($0\% \sigma_{\text{sys_un}}$)		47.3	Significance ($0\% \sigma_{\text{sys_un}}$)		37.2
Signal significance ($2\% (5\%) \sigma_{\text{sys_un}}$)		42.4 (30.3)	Signal significance ($2\% (5\%) \sigma_{\text{sys_un}}$)		36.7 (34.6)

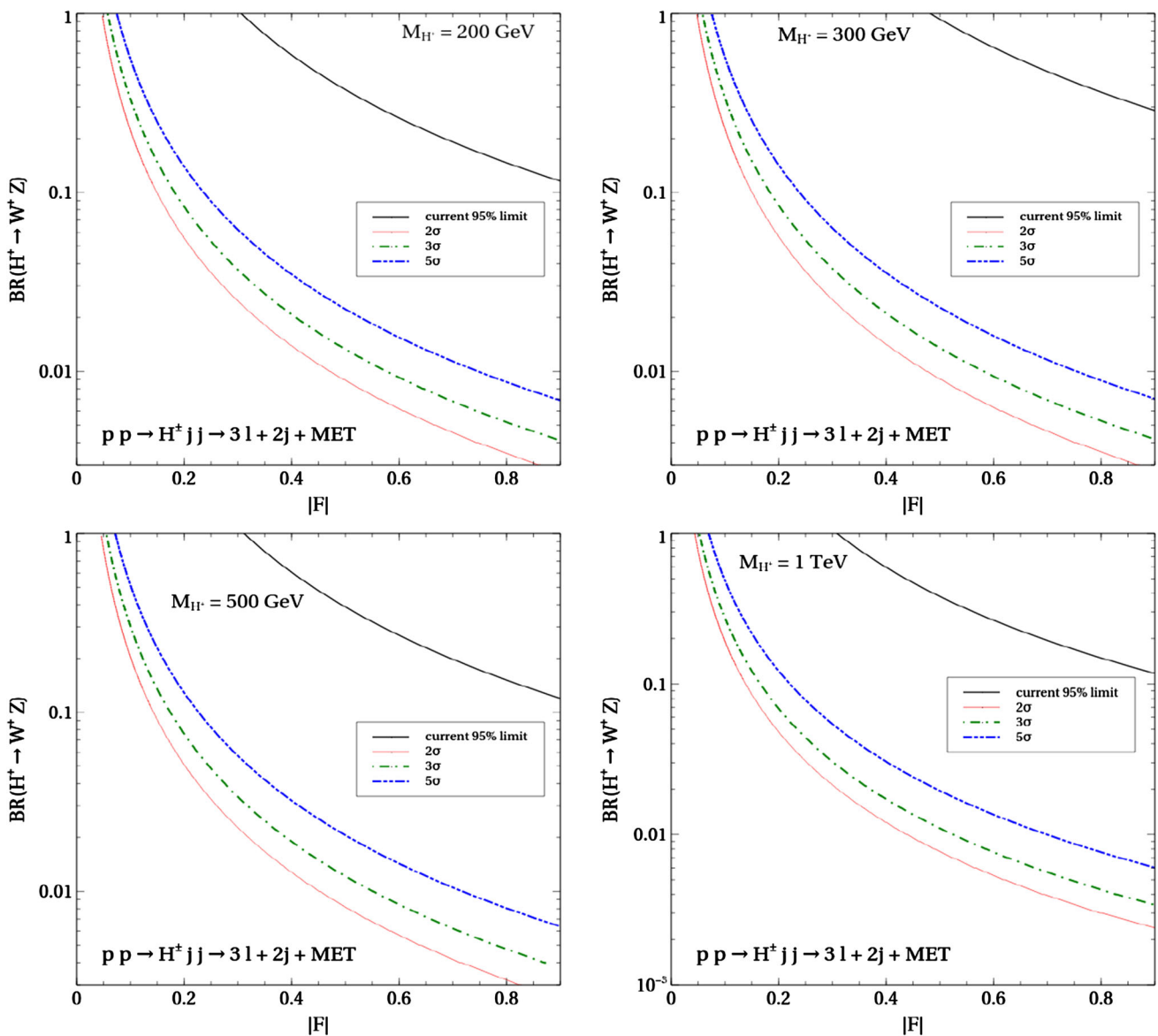


Fig. 4 The 2σ , 3σ and 5σ contours for the $pp \rightarrow H^\pm jj, H^\pm \rightarrow W^\pm Z$ signal in the $|F|$ - $BR(H^\pm \rightarrow W^\pm Z)$ plane for different M_{H^\pm} . The region above the black curve is ruled out at 95% confidence level (CL) by the CMS search for $pp \rightarrow H^\pm jj, H^\pm \rightarrow W^\pm Z$ channel

sen signal benchmarks and background processes are given in Table 9. We impose the following generation-level cuts while generating these backgrounds to better handle the statistics for large backgrounds :

$$\begin{aligned}
 p_T^{j,b} &> 20 \text{ GeV}, p_T^l > 10 \text{ GeV}, \\
 |\eta_{j,b,l}| &< 5.0, \Delta R_{j,b,l} > 0.2
 \end{aligned}
 \tag{13}$$

In addition to the generation-level cuts we add stronger trigger-level cuts on $|\eta_{j,b,l}|$ as: $|\eta_{j,b,l}| < 2.5$. To first perform a rectangular CBA, a set of relevant kinematic variables are constructed and their distributions are observed. Here we mostly present those distributions that illustrate the features

of VBF topology and shall apply suitable cuts on the variables for maximising the significance.

- B_1 and B_2 : The absence of hadronic activity in the central region is evident from the distributions of $M_{j_1 j_2}, |\Delta\eta_{j_1 j_2}|$. The distribution of $|\Delta\eta_{j_1 j_2}|$ peaks at a larger value for the signal as compared to the background processes. Consequently $M_{j_1 j_2}$ is distributed towards higher mass values. The more separated the two jets are, the larger will be their invariant mass. We also explicitly put a central jet-veto condition, implying the veto on the additional production of jets in the central region (between two forward and backward jets).

Table 9 The cross sections of signal and backgrounds for the process $pp \rightarrow H^\pm jj \rightarrow tbjj \rightarrow 2b + 1l + 2j + \cancel{E}_T$. The signal cross sections are computed for the $(F, \text{BR}(H^+ \rightarrow t\bar{b})) = (0.4, 0.4)$ reference point

Signal/backgrounds	Process	Cross section σ (fb)
Signal		
BP1 ($M_{H^+} = 200$ GeV)		123.37
BP2 ($M_{H^+} = 300$ GeV)	$pp \rightarrow H^\pm jj \rightarrow tbjj \rightarrow 2b + 1l + 2j + \cancel{E}_T$	76.93
BP3 ($M_{H^+} = 500$ GeV)		37.04
BP4 ($M_{H^+} = 1$ TeV)		10.62
Backgrounds		
	$pp \rightarrow t\bar{t}$ (semileptonic) (NNLO)	906843.5
	$pp \rightarrow t\bar{t}$ (leptonic) (NNLO)	245010.26
	$pp \rightarrow 2bl\nu jj$ (LO)	69691
	$pp \rightarrow tW + j$ (LO)	19733.25
	$pp \rightarrow t\bar{t}h$ (NLO)	2860
	$pp \rightarrow t\bar{t}Z$ (NLO)	3477.02
	$pp \rightarrow t\bar{t}W$ (LO)	986.58

- B_3 : Similar to the previous channel, the charged Higgs mass can be reconstructed for this case too since there is only one neutrino in the final state that comes from the decay of the W . First, we reconstruct the four top masses from two possible choices of pairing with bottom quark and the two possible solution corresponding to the z -component of \cancel{E}_T ($\cancel{E}_{T,z}$) as described in Sect. 4.1. Here we choose those combinations for which the reconstructed top mass is closest to $M_t = 173$ GeV. After that we construct the invariant mass of whole $2bl\nu$ -system $M_{2bl\nu}$, which should peak around the charged Higgs mass (M_{H^+}) for the signal events. This particular variable plays a crucial role in signal background separation, since for backgrounds the reconstructed mass will not peak around M_{H^+} .
- B_4 : We construct an observable called M_{eff} which is defined as the scalar sum of transverse momenta of all visible particles and \cancel{E}_T . This variable helps us separate signal from background especially in the high M_{H^+} region, because the decay products of a heavy charged Higgs will naturally be boosted rendering higher M_{eff} for the whole system.
- B_5 : We also utilise the contranverse mass variable, $M_{CT}(a, b)$ [71] which is an invariant quantity for two objects a and b having contra-linear (opposite in direction) and equal magnitude boost. This variable is defined as,

$$M_{CT}^2(a, b) = M^2(a) + M^2(b) + 2(E_T(a)E_T(b) + \vec{p}_T(a) \cdot \vec{p}_T(b)).$$

Here, $M(a)$ and $\vec{p}_T(a)$ corresponds to the invariant mass and transverse momentum vector respectively for the object a , whereas the transverse energy, E_T is defined as $\sqrt{|\vec{p}_T|^2 + M^2}$. Since in case of the signal $b\bar{b}$ and l come from the decay of charged Higgs, the end point

of $M_{CT}(b\bar{b}, l)$ distribution in this case will indicate the charged Higgs mass in the large M_{H^+} limit. The reason is the following : $M_{CT}(b\bar{b}, l)$ is constructed from the transverse momenta of the $b\bar{b}$ and l system where both of them are bounded from above by $M_{H^+}/2$ by construction. Therefore, $M_{CT}(b\bar{b}, l)$ can take a maximum value of M_{H^+} , the remaining terms being negligible compared to M_{H^+} . We can see from Fig. 5, this variable possesses good discriminating power. Although we have not used this $M_{CT}(b\bar{b}, l)$ in the cut-based analysis since it becomes redundant after applying cuts on the other discriminating variables, because of its correlation with variables such as $M_{2bl\nu}$, we have utilised this variable as an input for our BDTD analysis which will be discussed shortly.

The optimised cuts on the aforementioned variables for each of the benchmark points are given in Table 10. These cuts are applied to select the events over and above the basic generation-level and trigger-level cuts discussed above.

Tables 12, 13, 14 and 15 show the cut-flow for the signal and the background processes, yielding a fair indication of the efficiency of each cut. We have also calculated the projected significance for each benchmark point at 27 TeV LHC with 15 ab^{-1} luminosity.

We can see in Tables 12, 13, 14 and 15 that BP2 fares best in terms of signal significance, followed by BP1, BP3 and BP4. Therefore, BP1 which has the lowest mass of charged Higgs, has lowest discriminating capacity between the signal and background. However, its large cross-section enables us to achieve substantial signal significance. On the other hand, BP4, which corresponds to the heaviest charged Higgs has the best discriminating power among all the BPs. But its meagre production cross-section makes it difficult to obtain a good significance. However, as we can rely on various good separation variables in case of BP4, we expect significant

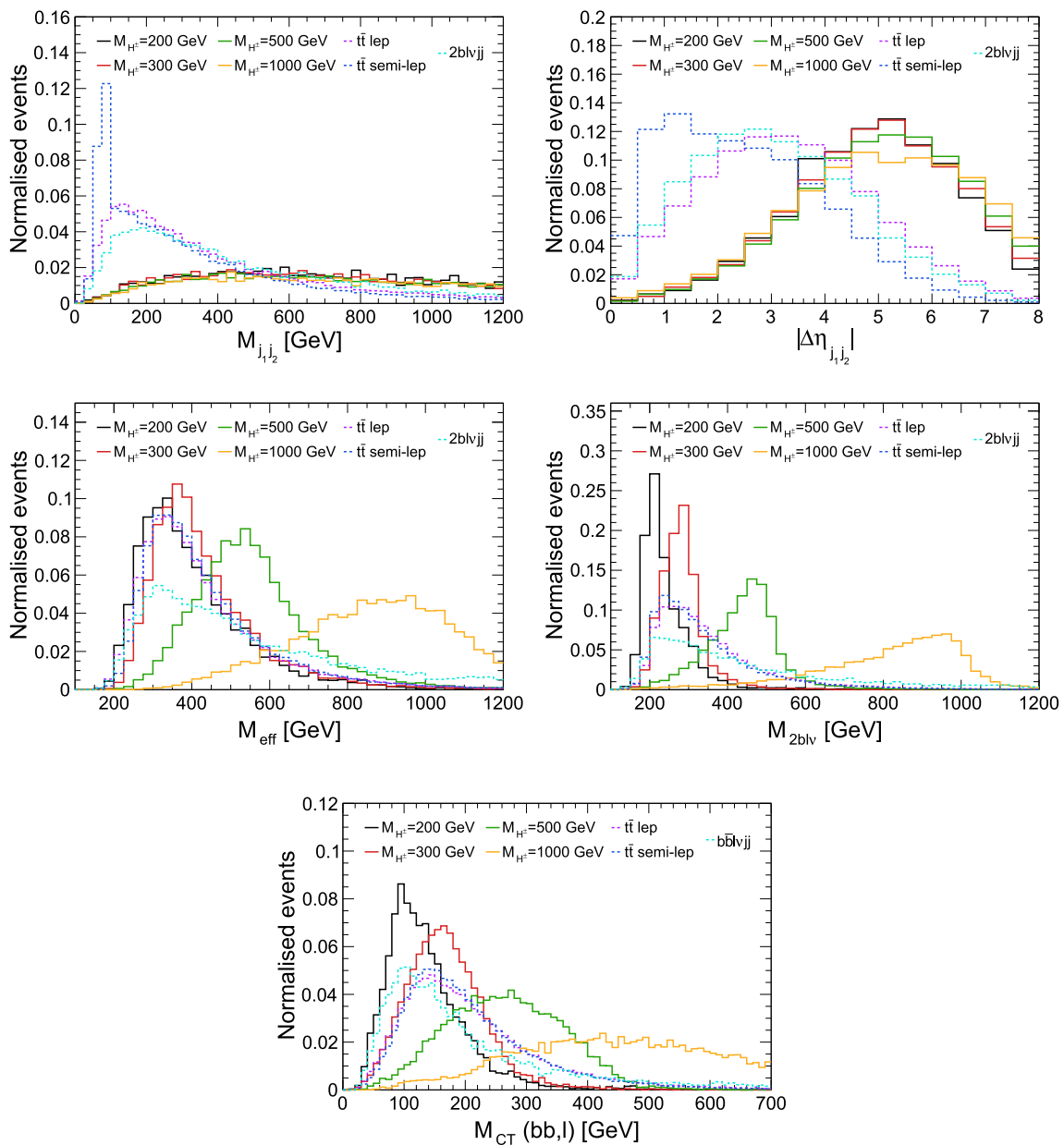


Fig. 5 Normalised distributions of $M_{j_1 j_2}$, $|\Delta\eta_{j_1 j_2}|$, M_{eff} , M_{2blv} and $M_{CT}(bb, l)$ for the $2b + 1l + 2j + \cancel{E}_T$ channel

Table 10 The optimised selection cuts for the $2b + 1l + 2j + \cancel{E}_T$ channel

M_{H^+}	B_1	B_2	B_3	B_4
200 GeV	$ \Delta\eta_{j_1 j_2} > 3$	$M_{j_1 j_2} > 500$ GeV	$100 \text{ GeV} < M_{H^+} < 300$ GeV	–
300 GeV	$ \Delta\eta_{j_1 j_2} > 3$	$M_{j_1 j_2} > 500$ GeV	$100 \text{ GeV} < M_{H^+} < 300$ GeV	–
500 GeV	$ \Delta\eta_{j_1 j_2} > 3$	$M_{j_1 j_2} > 500$ GeV	$M_{H^+} > 350$ GeV	$M_{eff} > 400$ GeV
1 TeV	$ \Delta\eta_{j_1 j_2} > 3$	$M_{j_1 j_2} > 500$ GeV	$M_{H^+} > 650$ GeV	$M_{eff} > 750$ GeV

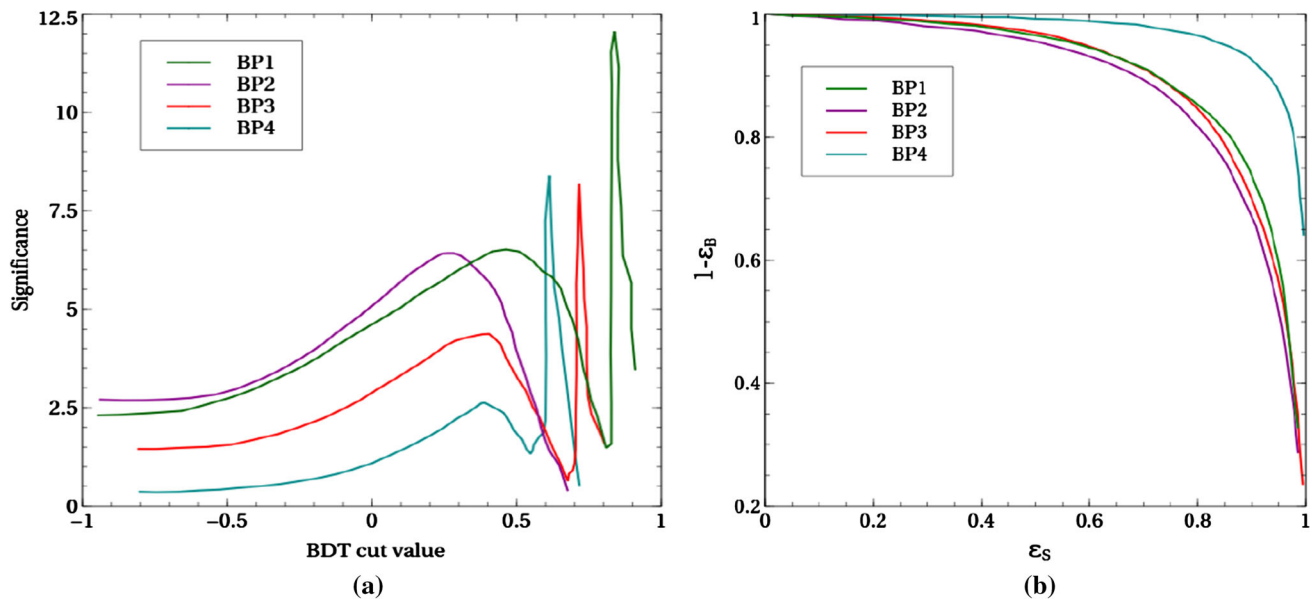
improvement over the cut-based analysis when we perform multivariate analysis. Evidently, for BP2 and BP3 there are good optimisations between production cross section and

signal-background separation and consequently they yield considerable significance even with the rectangular CBA.

Next we proceed to perform the MVA using BDTD algorithm with the hope of improving the significance with

Table 11 Tuned BDT parameters for BP1, BP2, BP3 and BP4 for the $2b + 1l + 2j + \cancel{E}_T$ channel

	NTrees	MinNodeSize	MaxDepth	nCuts	KS-score for signal (background)	BDT Score
BP1	40	3%	2	40	0.31 (0.145)	0.4
BP2	100	3%	2	20	0.396 (0.236)	0.23
BP3	100	3%	2	20	0.335 (0.43)	0.25
BP4	100	3%	2	20	0.029 (0.044)	0.32

**Fig. 6** (a) Variation of significance with BDT-score for $2b + 1l + 2j + \cancel{E}_T$ channel. (b) ROC curves for chosen benchmark points for $2b + 1l + 2j + \cancel{E}_T$ channel

respect to that obtained from CBA. Details of BDTD algorithm along with the definitions of the BDTD parameters are already discussed in Sect. 4.1. Thus we shall avoid repeating that here. Let us move on to Table 11, where all the tuned BDT parameters like NTrees, MinNodeSize, MaxDepth, nCuts, KS-scores (both for signal and backgrounds) and BDT score for four benchmarks are tabulated. The signal and background distributions along with their KS-scores are depicted in Fig. 19 in Appendix A. From this figure it can be inferred that the best possible signal background separation occurs for BP4. The variation of significance with BDT cut value or BDT score, depicted in Fig. 6(a) shows that the significance becomes highest for a particular value of BDT score. While computing the final signal significance, we use the BDT cut values for which the significances are maximised for four benchmarks. Fig. 6(b) represents the ROC curves for four benchmarks. It can be clearly seen that the background rejection efficiency for BP4 is best compared to the rest. In spite of having the best background rejection efficiency, BP4 has the lowest signal significance owing to small signal cross section (Table 9). According to the ability to differentiate between the signal and background, let us choose following thirteen

kinematic variables:

$$M_{bb}, p_T^{bb}, \Delta R_{bb}, M_{j_1 j_2}, \eta_{j_1 j_2}, |\Delta \eta_{j_1 j_2}|, M_{eff}, \Delta \phi_{l \cancel{E}_T}, \Delta \phi_{bb, l j_1 j_2}, M_{CT}(bb, l), M_{bbj_1}, M_{bbj_2}, M_{2bl\nu}. \quad (14)$$

where $\eta_{j_1 j_2}$ and $|\Delta \eta_{j_1 j_2}|$ are the pseudorapidity of the system of two leading light jets and $\Delta \eta_{j_1 j_2}$ between the two leading jets respectively. $\Delta \phi_{bb, l j_1 j_2}$ is the azimuthal angle separation between the two b -jet system and the system of lepton with two leading light jets, and the rest of the variables have their usual meaning. The most important variables to distinguish between the signal and backgrounds are $\Delta R_{bb}, M_{j_1 j_2}, \eta_{j_1 j_2}, M_{eff}, |\Delta \eta_{j_1 j_2}|, M_{bbj_1}, M_{bbj_2}, M_{2bl\nu}$. While doing the analysis, we have set $F = 0.4$ and we fix the branching ratio of the decay $H^+ \rightarrow t\bar{b}$ to be 40%. The normalised distributions of the best kinematic variables for different M_{H^+} are shown in Fig. 5. After doing the BDTD analysis, we summarise the results in Table 16.

Comparing the results obtained from BDTD analysis (Table 16) and those from cut-based analysis (Table 12, 13, 14, 15) we can see that BP1 is hardly improved by the BDTD analysis. Since the kinematic variables do not offer a good separation in this case, the BDTD will per-

Table 12 Signal and background yields after applying the selection cuts and projected signal significance for BP1 with 15 ab^{-1} integrated luminosity. The signal yields are computed for the $(F, \text{BR}(H^+ \rightarrow t\bar{b})) = (0.4, 0.4)$ reference point

$M_{H^+} = 200 \text{ GeV}$	NEV ($\mathcal{L} = 15 \text{ ab}^{-1}$)		
	B_1	B_2	B_3
Signal	33,079	27,362	24,870
$t\bar{t}$ semileptonic	4.9×10^7	1.7×10^7	9.6×10^6
$t\bar{t}$ leptonic	3.6×10^7	1.5×10^7	7.7×10^6
$2bl\nu jj$	5.2×10^6	2.9×10^6	811360
tW	188,553	65,018	19,506
$t\bar{t}h$	30,598	12,777	4371
$t\bar{t}Z$	73,202	37,124	13,595
$t\bar{t}W$	16,703	4898	2261
Signal yield = 24,870	Total background yield = 1.8×10^7		Signal significance (0% $\sigma_{\text{sys_un}}$) = 5.9 Signal significance (2% (5%) $\sigma_{\text{sys_un}}$) = 0.07 (0.03)

Table 13 Signal and background yields after applying the selection cuts and projected signal significance for BP2 with 15 ab^{-1} integrated luminosity. The signal yields are computed for the $(F, \text{BR}(H^+ \rightarrow t\bar{b})) = (0.4, 0.4)$ reference point

$M_{H^+} = 300 \text{ GeV}$	NEV ($\mathcal{L} = 15 \text{ ab}^{-1}$)		
	B_1	B_2	B_3
Signal	48,351	39,091	33,816
$t\bar{t}$ semileptonic	4.9×10^7	1.7×10^7	9.6×10^6
$t\bar{t}$ leptonic	3.6×10^7	1.5×10^7	7.7×10^6
$2bl\nu jj$	5.2×10^6	2.9×10^6	811,360
tW	188,553	65,018	19,506
$t\bar{t}h$	30,598	12,777	4371
$t\bar{t}Z$	73,202	37,124	13,595
$t\bar{t}W$	16,703	4898	2261
Signal yield = 33,816	Total background yield = 1.8×10^7		Signal significance (0% $\sigma_{\text{sys_un}}$) = 8.0 Signal significance (2% (5%) $\sigma_{\text{sys_un}}$) = 0.09 (0.04)

Table 14 Signal and background yields after applying the selection cuts and projected signal significance for BP3 with 15 ab^{-1} integrated luminosity. The signal yields are computed for the $(F, \text{BR}(H^+ \rightarrow t\bar{b})) = (0.4, 0.4)$ reference point

$M_{H^+} = 500 \text{ GeV}$	NEV ($\mathcal{L} = 15 \text{ ab}^{-1}$)			
	B_1	B_2	B_3	B_4
Signal	25,195	21,194	19,484	17,586
$t\bar{t}$ semileptonic	3.1×10^7	1.1×10^7	5.6×10^6	5.1×10^6
$t\bar{t}$ leptonic	1.6×10^7	6.5×10^6	3.9×10^6	3.1×10^6
$2bl\nu jj$	5.2×10^6	2.9×10^6	2.3×10^6	1.9×10^6
tW	188553	65,018	52,015	45,513
$t\bar{t}h$	30,598	12,777	9079	7734
$t\bar{t}Z$	73,202	37,124	27,189	23,529
$t\bar{t}W$	16,703	4898	3140	2763
Signal yield = 17,586	Total background yield = 1.0×10^7		Signal significance (0% $\sigma_{\text{sys_un}}$) = 5.6 Signal significance (2% (5%) $\sigma_{\text{sys_un}}$) = 0.09 (0.04)	

Table 15 Signal and background yields after applying the selection cuts and projected signal significance for BP4 with 15 ab^{-1} integrated luminosity. The signal yields are computed for the $(F, \text{BR}(H^+ \rightarrow t\bar{b})) = (0.4, 0.4)$ reference point

$M_{H^+} = 1 \text{ TeV}$	NEV ($\mathcal{L} = 15 \text{ ab}^{-1}$)			
	B_1	B_2	B_3	B_4
Signal	6466	5553	5136	4149
$t\bar{t}$ semileptonic	3.1×10^7	1.1×10^7	1.8×10^6	679093
$t\bar{t}$ leptonic	1.6×10^7	6.5×10^6	872734	269754
$2bl\nu jj$	5.2×10^6	2.9×10^6	1.5×10^6	1.0×10^6
tW	188,553	65,018	39,011	26,007
$t\bar{t}h$	30,598	12,777	4371	3362
$t\bar{t}Z$	73,202	37,124	10,458	5752
$t\bar{t}W$	16,703	4898	1381	879
Signal yield = 4149	Total background yield = 1.9×10^6		Signal significance ($0\% \sigma_{\text{sys_un}}$) = 3.0	
			Signal significance (2% (5%) $\sigma_{\text{sys_un}}$) = 0.11 (0.04)	

Table 16 The signal and background yields at 15 ab^{-1} for $M_{H^+} = 200 \text{ GeV}$, 300 GeV , 500 GeV and 1 TeV along with signal significances for the $2b + 1l + 2j + \cancel{E}_T$ channel after the BDTD analysis. The signal yields are computed for the $(F, \text{BR}(H^+ \rightarrow t\bar{b})) = (0.4, 0.4)$ reference point

	$M_{H^+} = 200 \text{ GeV}$		$M_{H^+} = 300 \text{ GeV}$		
	Process	Yield at 15 ab^{-1}	Process	Yield at 15 ab^{-1}	
Background	$t\bar{t}$ lep	2,914,397	Background	$t\bar{t}$ lep	6,617,115
	$t\bar{t}$ semi-lep	8,977,751		$t\bar{t}$ semi-lep	18,207,150
	$2bl\nu jj$	797,091		$2bl\nu jj$	1,301,479
	tW	55,272		tW	108,774
	$t\bar{t}h$	16,688		$t\bar{t}h$	37,645
	$t\bar{t}Z$	13,821		$t\bar{t}Z$	30,693
	$t\bar{t}W$	1339		$t\bar{t}W$	2952
	Total	12,776,359		Total	26,305,808
Signal		23,261	Signal		52,583
Signal significance ($0\% \sigma_{\text{sys_un}}$)		6.5	Signal significance ($0\% \sigma_{\text{sys_un}}$)		10.2
Signal significance (2% (5%) $\sigma_{\text{sys_un}}$)		0.09 (0.04)	Signal significance (2% (5%) $\sigma_{\text{sys_un}}$)		0.1 (0.04)
	$M_{H^+} = 500 \text{ GeV}$		$M_{H^+} = 1 \text{ TeV}$		
	Process	Yield at 15 ab^{-1}	Process	Yield at 15 ab^{-1}	
Background	$t\bar{t}$ lep	3,914,039	Background	$t\bar{t}$ lep	356,490
	$t\bar{t}$ semi-lep	10,555,658		$t\bar{t}$ semi-lep	1,197,033
	$2bl\nu jj$	1,547,140		$2bl\nu jj$	899,014
	tW	95,951		tW	87,108
	$t\bar{t}h$	36,787		$t\bar{t}h$	11,004
	$t\bar{t}Z$	35,596		$t\bar{t}Z$	11,292
	$t\bar{t}W$	2568		$t\bar{t}W$	451
	Total	16,187,739		Total	2,562,392
Signal		54,387	Signal		42,525
Signal significance ($0\% \sigma_{\text{sys_un}}$)		13.5	Signal significance ($0\% \sigma_{\text{sys_un}}$)		26.5
Signal significance (2% (5%) $\sigma_{\text{sys_un}}$)		0.17 (0.07)	Signal significance (2% (5%) $\sigma_{\text{sys_un}}$)		0.82 (0.33)

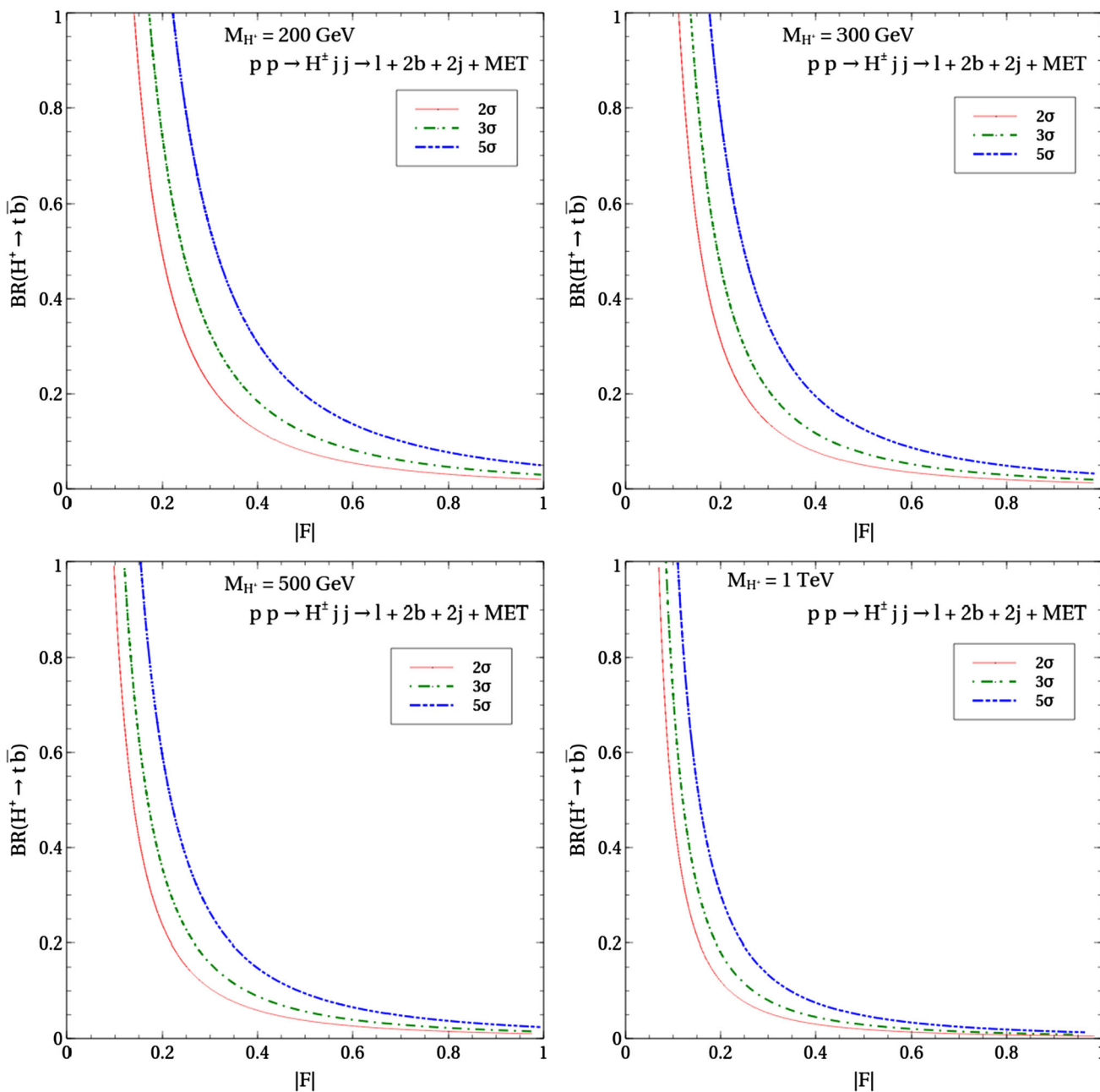


Fig. 7 The 2σ , 3σ and 5σ contours for the $pp \rightarrow H^\pm jj, H^+ \rightarrow t\bar{b}$ signal in the $|F|$ - $BR(H^+ \rightarrow t\bar{b})$ plane for different M_{H^+}

form marginally better than an optimized cut-based analysis. The results improve slightly in case of BP2. The improvement becomes striking in case of BP3 and BP4, because these benchmarks correspond to observables with significant discriminating power. Considering 2% and 5% systematic uncertainties, the significances has also been calculated and tabulated in Table 16.

Similar to what was done for the previous channel, we next display the contours of constant signal significance in the $|F|$ - $BR(H^\pm \rightarrow t\bar{b})$ plane in Fig. 7.

4.3 The $5l + \cancel{E}_T$ channel

With the results of the VBF analyses in hand, we turn our attention to the $pp \rightarrow ZH^\pm \rightarrow 5l + \cancel{E}_T$ channel. To elaborate a bit, the H^\pm here is produced in association with a Z -boson via an s -channel exchange of the W -boson and it subsequently leads to the hadronically quiet $H^\pm \rightarrow W^\pm Z \rightarrow 3l + \cancel{E}_T$ decay cascade. The other Z -boson also decays leptonically. The Feynman diagram corresponding to this signal can be found in Fig.1(c). Throughout this

Table 17 Cross sections of signal and backgrounds for the process $pp \rightarrow ZH^\pm \rightarrow W^\pm ZZ \rightarrow 5l + \cancel{E}_T$. The signal cross sections are computed for the $(F, BR(H^+ \rightarrow W^+Z)) = (0.4, 0.4)$ reference point

Signal/backgrounds	Process	Cross section σ (fb)
Signal		
BP1 ($M_{H^+} = 200$ GeV)	$pp \rightarrow ZH^\pm \rightarrow W^\pm ZZ \rightarrow 5l + \cancel{E}_T$	2.64×10^{-2}
BP2 ($M_{H^+} = 300$ GeV)		6.54×10^{-3}
BP3 ($M_{H^+} = 500$ GeV)		9.84×10^{-4}
BP4 ($M_{H^+} = 1$ TeV)		6.26×10^{-5}
Backgrounds		
	$pp \rightarrow W^\pm ZZ \rightarrow 5l + \cancel{E}_T$	7.93×10^{-2} (LO)
	$pp \rightarrow hW^\pm \rightarrow 5l + \cancel{E}_T$	6.85×10^{-2} (LO)
	$pp \rightarrow hZ \rightarrow 6l$	1.13×10^{-2} (LO)
	$pp \rightarrow t\bar{t}h \rightarrow 6l + 2b + \cancel{E}_T$	1.42×10^{-2} (NLO)

Table 18 Tuned BDT parameters for BP1, BP2 and BP3 for the $5l + \cancel{E}_T$ channel

	NTrees	MinNodeSize	MaxDepth	nCuts	KS-score for signal (background)	BDT score
BP1	160	4%	2.0	30	0.023 (0.051)	-0.02
BP2	180	3%	2.0	39	0.323 (0.943)	0.06
BP3	200	3%	2.0	40	0.981 (0.121)	0.17

analysis, we remain agnostic to the fact that the prospects of observing an H^+ in this channel could be low and this would be attributed to a small signal cross section(s).

Background processes leading to an exactly $5l + \cancel{E}_T$ final state are $pp \rightarrow W^\pm ZZ$ and $pp \rightarrow hW^\pm$. Sub-leading backgrounds come from $pp \rightarrow hZ \rightarrow 6l$ and $pp \rightarrow t\bar{t}h \rightarrow 6l + 2b + \cancel{E}_T$. Mis-identification of a lepton as missing energy can lead to a $5l + \cancel{E}_T$ state originating from the former. As for the latter, obtaining the same final state as the signal would entail mis-identification of one lepton and 2 b -jets. We show the cross sections for the signal and the backgrounds in Table 17.

BP4 is excluded from the subsequent analysis owing to the small signal cross section. We start by vetoing the b -jets and τ -jets in the final state, so that the final state (comprising of five leptons) is completely leptonic. Here by lepton we mean e, μ and have taken all possible combinations of those five leptons leading to two same flavour opposite sign (SFOS) pairs and one isolated lepton.

Since the MVA was found to outperform the CBA for the two VBF signals, we choose to omit the CBA for this process. Different BDT parameters used to carry out the MVA, are given in Table 18. Figure 20 in Appendix A depicts the distribution for signal and backgrounds along with the KS-scores for this channel. In Fig. 9(a), (b) we show the variation of significance with BDT score and ROC curves for three benchmarks respectively. It can be seen that the background rejection efficiency increases with increasing M_{H^+} . The following twenty kinematic variables are chosen according to

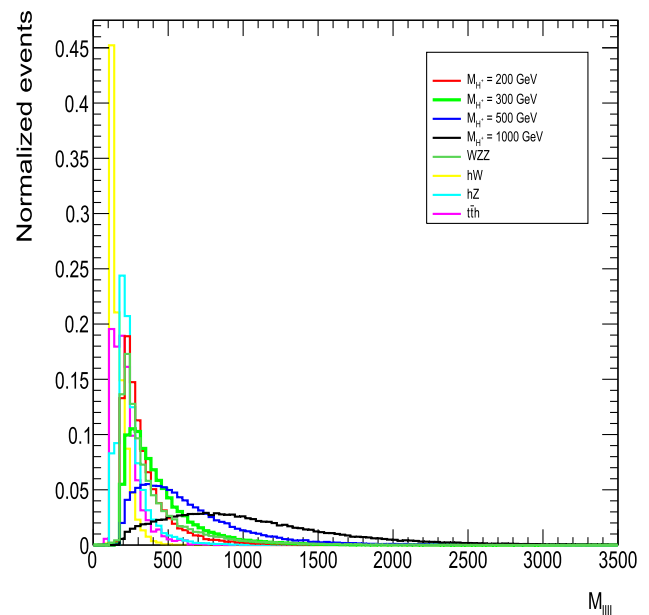


Fig. 8 Normalised distribution of M_{III} for the $5l + \cancel{E}_T$ channel

the degree of distinguishing capability to initiate the MVA.

$$\begin{aligned}
 & (M_{II})_1, (M_{II})_2, M_{III}, M_{inv}^{WZ}, \cancel{E}_T, \Delta R_{l_1 l_2}, \Delta R_{l_1 l_3}, \Delta R_{l_1 l_4}, \\
 & \Delta R_{l_1 l_5}, \Delta R_{l_2 l_3}, \Delta R_{l_2 l_4}, \\
 & \Delta R_{l_2 l_5}, \Delta R_{l_3 l_4}, \Delta R_{l_3 l_5}, \Delta R_{l_3 l_5}, \Delta \phi_{l_1 \cancel{E}_T}, \\
 & \Delta \phi_{l_2 \cancel{E}_T}, \Delta \phi_{l_3 \cancel{E}_T}, \Delta \phi_{l_4 \cancel{E}_T}, \Delta \phi_{l_5 \cancel{E}_T}
 \end{aligned} \tag{15}$$

Here we reconstruct the two Z -boson invariant masses $(M_{II})_1$ and $(M_{II})_2$ by combinatorially identifying the correspond-

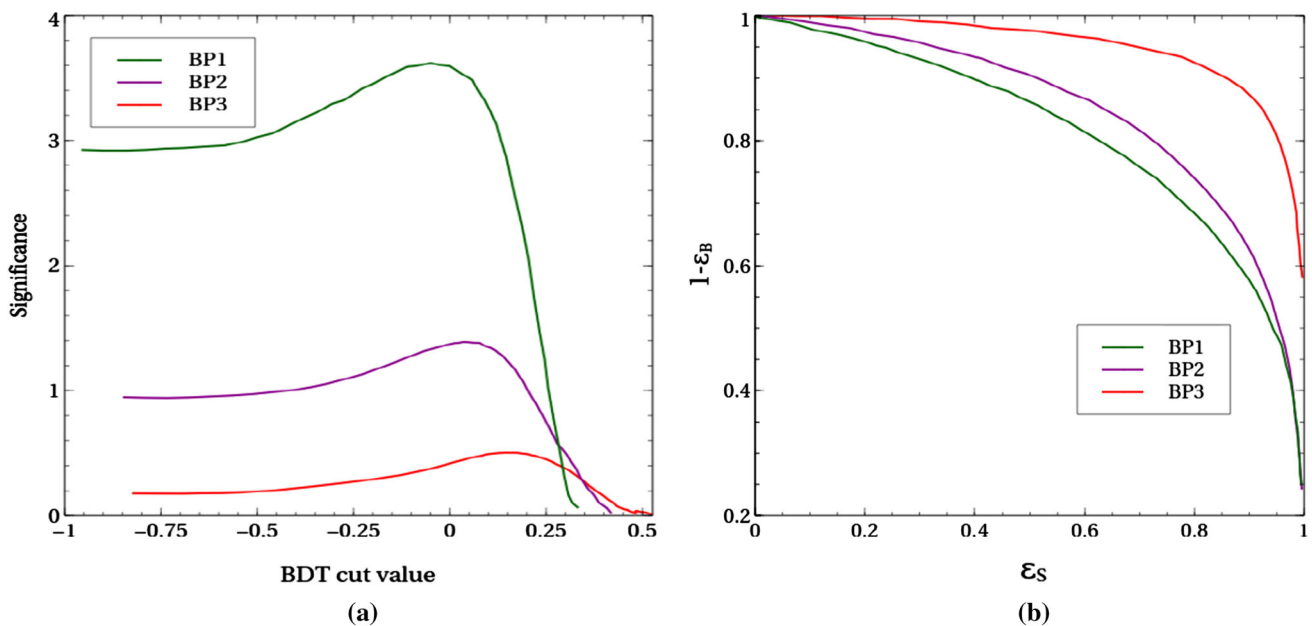


Fig. 9 (a) Variation of significance with BDT-score for $5l + \cancel{E}_T$ channel, (b) ROC curves for chosen benchmark points for $5l + \cancel{E}_T$ channel

ing two SFOS lepton pairs. Any cut on these is expected to suppress the hW^\pm and $t\bar{t}h$ backgrounds appropriately that do not involve a pair of on-shell Z-bosons. Next, the invariant mass of the two pairs of SFOS lepton system (M_{llll}), originating from the decay of two Z-bosons, is constructed. Since for the hW^\pm background, h decays into ZZ^* , the distribution of M_{llll} peaks around 125 GeV in Fig. 8. Thus a veto cut on M_{llll} around 125 GeV for all values of M_{H^+} would help suppressing the aforementioned background to a large extent. Similarly to what was done for the $H^\pm jj \rightarrow W^\pm Zjj$ channel, we construct the invariant mass of the $lll\nu$ system (M_{inv}^{WZ}) that comes from H^\pm . For $W^\pm ZZ$ background, $W^\pm Z$ are not originated from the decay of a single mother particle as in the signal. Therefore one can rely on this variable which has substantial discriminatory power between the signal and the backgrounds. Here $\Delta\phi_{l_i \cancel{E}_T}$ is the azimuthal angle between l_i and the missing transverse energy vector. Rest of the aforementioned kinematic variables have been defined earlier. Among these twenty variables, $(M_{ll})_1, (M_{ll})_2, M_{llll}, M_{inv}^{WZ}, \Delta R_{l_1 l_2}, \Delta R_{l_1 l_3}, \cancel{E}_T$ turn out to be the best performing having high discerning ability to separate signal and backgrounds. Corresponding yields for signal and backgrounds at $\mathcal{L} = 15 \text{ ab}^{-1}$ for $M_{H^+} = 200 \text{ GeV}, 300 \text{ GeV}$ and 500 GeV along with the signal significances are given in Table 19. The maximum significance of 4.24 is predicted for $M_{H^+} = 200 \text{ GeV}$ following the BDTD analysis. The significance declines for the higher charged Higgs masses (Fig. 9). Significances with 2% and 5% systematic uncertainties are presented in Table 19.

Figure 10 displays the $2\sigma, 3\sigma$ and 5σ contours in the $|F|$ - $\text{BR}(H^+ \rightarrow W^+Z)$ plane. Upon comparing it with Fig. 4,

one concludes that for an H^+ decaying to the massive gauge bosons, ZH^+ production has a much lower reach compared to VBF production. To quote a few numbers, an H^+ of mass 500 GeV that corresponds to $|F| = 0.4$ can be discovered at 5σ for $\text{BR}(H^+ \rightarrow W^+Z) \gtrsim 3\%$ via the $3l + 2j + \cancel{E}_T$ final state. In contrast, the $5l + \cancel{E}_T$ final state demands $F \simeq 0.8$ and $\text{BR}(H^+ \rightarrow W^+Z) \simeq 100\%$ to attain the same discovery potential.

4.4 The $3l + 2b + \cancel{E}_T$ channel

This subsection contains the analysis for the signal where following production in association with a Z, the charged boson decays to tb . In addition to $Z \rightarrow ll$ decay, we have the $t \rightarrow bl\nu$ leptonic decay in this case. This gives rise to three lepton final state with two b -tagged jets and \cancel{E}_T . The dominant contribution to the background in this final state comes from the $t\bar{t}X$ type production where $X = h, Z, W^\pm$. The ZZZ and $W^\pm ZZ$ production, $Zh, W^\pm h$ and $b\bar{b}h$ are the sub-dominant backgrounds in this channel owing to their smaller cross section compared to the previous ones. We present the cross sections of chosen signal benchmarks and background processes in Table 20.

We generate all of these backgrounds with the application of following generation level cuts:

$$p_T^b > 20 \text{ GeV}, p_T^l > 10 \text{ GeV}, |\eta_{b,l}| < 5.0, \Delta R_{b,l} > 0.2. \tag{16}$$

Further, exactly two b -tagged jets and three isolated leptons with the aforementioned transverse momenta satisfying $|\eta_{b,l}| < 2.5$ are demanded (Fig. 11). Out of these three

Table 19 The signal and background yields at 15 ab⁻¹ for $M_{H^\pm} = 200$ GeV, 300 GeV and 500 GeV along with signal significances for the $5l + \cancel{E}_T$ channel after the BDTD analysis. The signal yields are computed for the $(F, \text{BR}(H^\pm \rightarrow W^\pm Z)) = (0.4, 0.4)$ reference point

$M_{H^\pm} = 200$ GeV			$M_{H^\pm} = 300$ GeV		
	Process	Yield at 15 ab ⁻¹		Process	Yield at 15 ab ⁻¹
Background	$W^\pm ZZ$	34	Background	$W^\pm ZZ$	18
	hW^\pm	3		hW^\pm	~ 0
	hZ	7		hZ	1
	$t\bar{t}h$	~ 0		$t\bar{t}h$	~ 0
	Total	44		Total	19
Signal ($pp \rightarrow H^\pm Z \rightarrow 5l + \cancel{E}_T$)		31	Signal ($pp \rightarrow H^\pm Z \rightarrow 5l + \cancel{E}_T$)		7
Significance (0% $\sigma_{\text{sys_un}}$)		4.24	Significance (0% $\sigma_{\text{sys_un}}$)		1.5
Signal significance (2% (5%) $\sigma_{\text{sys_un}}$)		4.2 (4.0)	Signal significance (2% (5%) $\sigma_{\text{sys_un}}$)		1.5 (1.48)

$M_{H^\pm} = 500$ GeV		
	Process	Yield at 15 ab ⁻¹
Background	$W^\pm ZZ$	3
	hW^\pm	~ 0
	hZ	~ 0
	$t\bar{t}h$	~ 0
	Total	3
Signal ($pp \rightarrow H^\pm Z \rightarrow 5l + \cancel{E}_T$)		1.3
Significance (0% $\sigma_{\text{sys_un}}$)		0.7
Signal significance (2% (5%) $\sigma_{\text{sys_un}}$)		0.7 (0.7)

leptons we first construct the invariant mass of the SFOS lepton pair, which must peak at M_Z . Then the remaining lepton along with the \cancel{E}_T and b -jets is used to reconstruct the charged Higgs mass. We apply the same technique to reconstruct M_{H^\pm} as described in Sect. 4.2. Next, we perform the MVA by adjusting the BDT parameters as mentioned in Table 21. The signal and background distributions and the KS-scores are depicted in Fig. 21 in Appendix A. The significance vs. BDT score plot has been presented in Fig. 12(a). Degree of rejecting the backgrounds can be identified from the ROC curves for three benchmarks in Fig. 12(b). Following the ranking of the kinematic variables provided by BDTD algorithm we choose the following twelve kinematic variables:

$$M_{bb}, \Delta R_{bb}, p_T^l, M_{ll}, \Delta, \phi_{ll}, \Delta\phi_{Zl_3}, p_{T,vis}^{H^\pm}, p_{T,vis}^{H^\pm Z}, \eta_{H^\pm Z}^{vis} \Delta\phi_{H^\pm Z}, M_{2bl\nu}, M_{CT}(H^\pm Z). \tag{17}$$

Here, p_T^l , M_{ll} and $\Delta\phi_{ll}$ are constructed from the two SFOS leptons which satisfy Z -mass criteria discussed at the beginning of this section, while the remaining third lepton refers to the l_3 in the kinematic variable $\Delta\phi_{Zl_3}$. M_{ll} and $M_{2bl\nu}$ are the reconstructed Z -boson mass and charged Higgs mass respectively. The $p_{T,vis}^{H^\pm}$ and $p_{T,vis}^{H^\pm Z}$ are the visible transverse momentum of the charged Higgs and total system (H^\pm and Z -boson) respectively. $\Delta\phi_{H^\pm Z}$

is the azimuthal angle separation between the charged Higgs and Z -boson system, whereas $M_{CT}(H^\pm Z)$ is the contranverse mass of the $H^\pm Z$ -system, constructed as defined in Sect. 4.2. The other kinematic variables have their usual meaning. Among all these kinematic variables, M_{bb} , ΔR_{bb} , p_T^l , $M_{2bl\nu}$, $M_{CT}(H^\pm Z)$, $p_{T,vis}^{H^\pm}$, $p_{T,vis}^{H^\pm Z}$ are the most important to maximise the signal significance. The results are summarised in Table 22. In addition, the signal significances considering 2% and 5% systematic uncertainty have been relegated in Table 22. Also, We show the normalised distributions of the kinematic variables having best discriminatory power between the signal and the backgrounds in Fig. 11.

After computing the signal significance for our proposed signal ($pp \rightarrow 3l + 2b + \cancel{E}_T$) corresponding to the BPs and a specific value of the coupling $F = 0.4$ and $\text{BR}(H^\pm \rightarrow t\bar{b}) = 40\%$, we present the contours of constant signal significance in the $|F|$ - $\text{BR}(H^\pm \rightarrow t\bar{b})$ plane in Fig. 13. A straightforward comparison with Fig. 7 establishes that for $H^\pm \rightarrow t\bar{b}$ too, the prospects of the ZH^\pm production process is much weaker compared to the VBF process in searching for an H^\pm . We quote a few numbers to put this into perspective. For $F = 0.4$, the VBF process offers 5σ observability for $\text{BR}(H^\pm \rightarrow t\bar{b}) \gtrsim 15\%$. This correspondingly weakens to $\text{BR}(H^\pm \rightarrow t\bar{b}) \gtrsim 70\%$ in case of ZH^\pm .

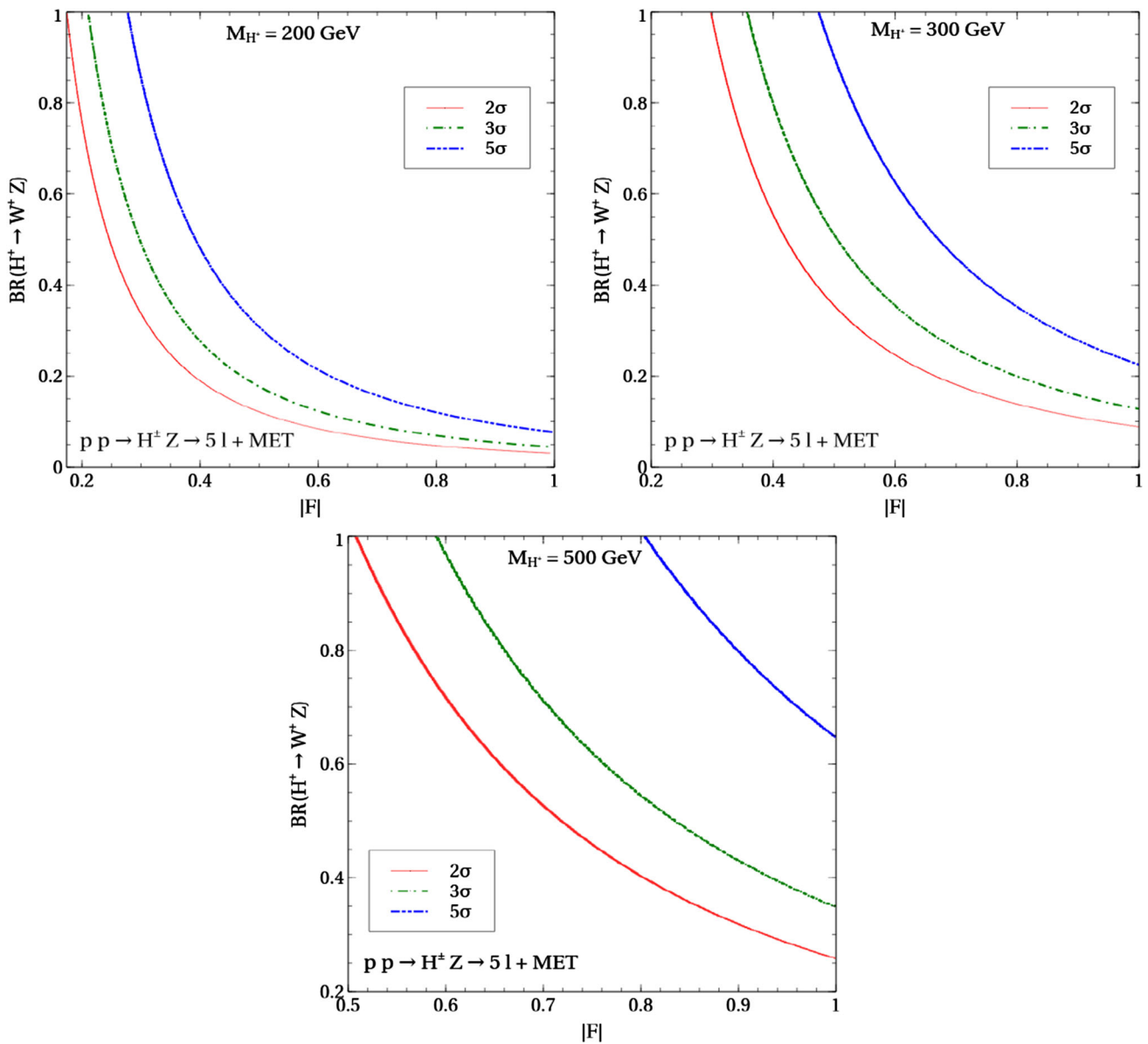


Fig. 10 The 2σ , 3σ and 5σ contours for the $pp \rightarrow ZH^\pm$, $H^+ \rightarrow W^+Z$ signal in the $|F|$ - $BR(H^+ \rightarrow W^+Z)$ plane for different M_{H^+}

5 Comparing the VBF sensitivities

In this section, we compare the sensitivities of the various channels in the $|F|$ - $|A_{tb}|$ plane. The magenta (sky blue) area in Fig. 14 is excluded by the H^+jj (tbH^\pm) search. Since the $pp \rightarrow jjH^\pm$ process statistically outperforms the $pp \rightarrow ZH^\pm$ process, we choose it to compare the sensitivities of the $H^\pm \rightarrow tb, W^\pm Z$ decay channels corresponding to the former. The dashed (solid) red, green and blue lines in Fig. 14 respectively correspond to the 2σ -exclusion, 3σ -discovery and 5σ -discovery contours for the $2b+1l+2j+\cancel{E}_T$ ($3l+2j+\cancel{E}_T$) channel. These contours are drawn by appropriately scaling the results of the multivariate analysis of either channel.

An inspection of Fig. 14 reveals that the $2b+1l+2j+\cancel{E}_T$ final state is useful in probing high values of $|F|$ for low $|A_{tb}|$ for all M_{H^+} . In case of $M_{H^+} = 200$ GeV, $|A_{tb}| \simeq 0.3$ can be probed at 5σ statistical yield for $|F| \gtrsim 0.28$. A higher statistical yield corresponding to a higher M_{H^+} expectedly enhances the sensitivity in the $|F| - |A_{tb}|$ plane. This is concurred by an inspection of Fig. 14. An H^+ of mass 500 GeV is seen to offer a 5σ observability when $|A_{tb}| \simeq 0.3$ and $|F| \gtrsim 0.2$.

On the other hand, the $3l+2j+\cancel{E}_T$ final state comes handy in probing simultaneously low values of $|F|$ and $|A_{tb}|$. The reason to this can be traced back to the fact that $\sigma_{3l+2j+\cancel{E}_T} \propto \frac{|F|^4}{|F|^2+|A_{tb}|^2}$ and therefore increasing (decreasing)

Table 20 The cross sections of signal and backgrounds for the process $pp \rightarrow H^\pm Z \rightarrow tbZ \rightarrow 3l + 2b + \cancel{E}_T$. The signal cross sections are computed for the $(F, \text{BR}(H^+ \rightarrow tb)) = (0.4, 0.4)$ reference point

Signal/backgrounds	Process	Cross section σ (fb)
Signal		
BP1 ($M_{H^+} = 200$ GeV)		0.9
BP2 ($M_{H^+} = 300$ GeV)	$pp \rightarrow H^\pm Z \rightarrow tbZ \rightarrow 2b + 3l + \cancel{E}_T$	0.224
BP3 ($M_{H^+} = 500$ GeV)		0.034
BP4 ($M_{H^+} = 1$ TeV)		0.0022
Backgrounds		
	$pp \rightarrow t\bar{t}h$ (NLO) [72]	2860.0
	$pp \rightarrow t\bar{t}Z$ (NLO) [73]	3477.02
	$pp \rightarrow t\bar{t}W$ (LO)	986.58
	$pp \rightarrow WZZ$ (LO)	0.5
	$pp \rightarrow ZZZ$ (LO)	0.07
	$pp \rightarrow Zh$ (NNLO QCD + NLO EW) [72]	0.057
	$pp \rightarrow Wh$ (NNLO QCD + NLO EW) [72]	0.185
	$pp \rightarrow b\bar{b}h$ (LO)	0.005

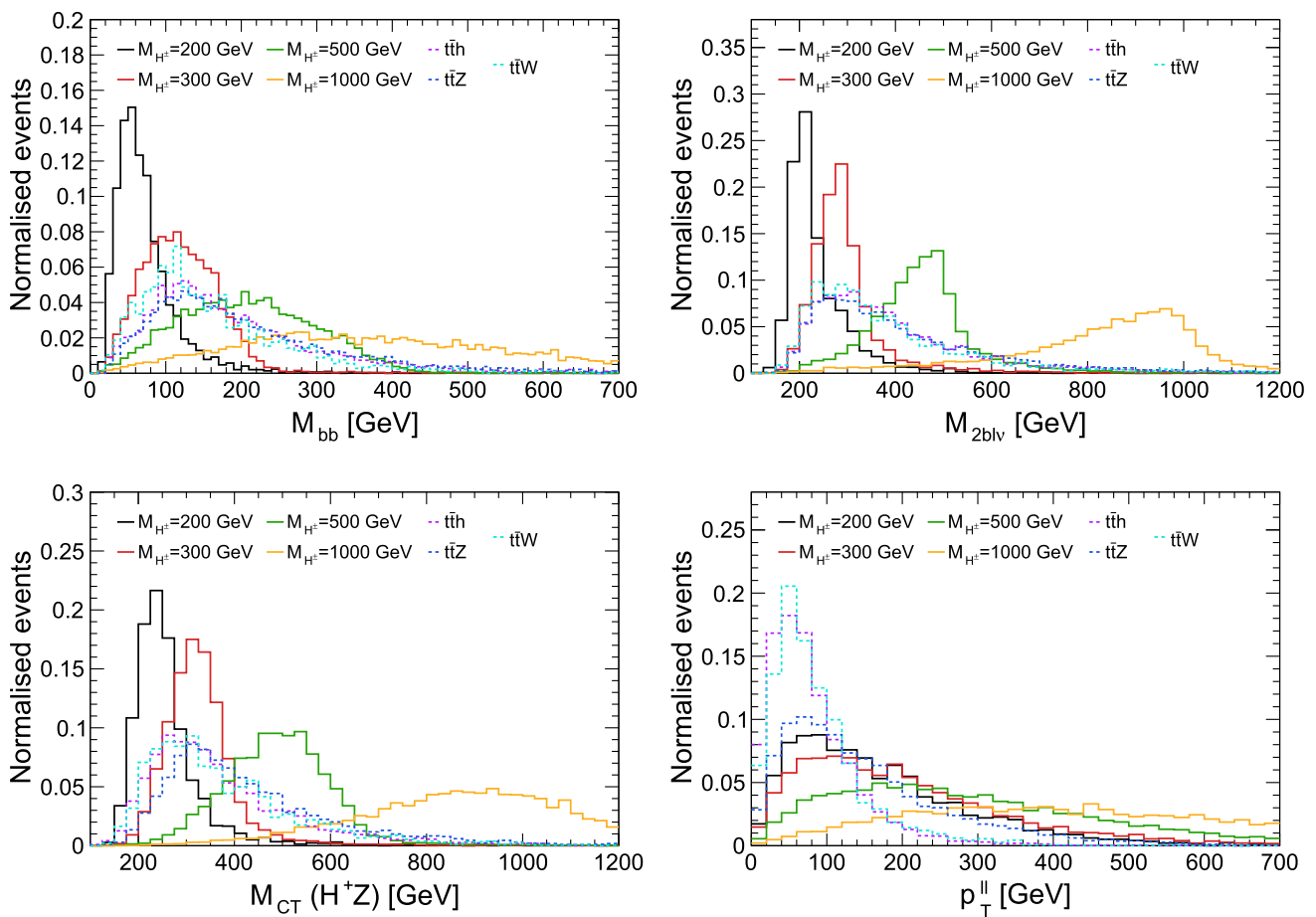
**Fig. 11** Normalised distributions of M_{bb} , M_{2blv} , $M_{CT}(H^+Z)$ and p_T^l for the $3l + 2b + \cancel{E}_T$ channel

Table 21 Tuned BDT parameters for BP1, BP2, BP3 and BP4 for the $3l + 2b + \cancel{E}_T$ channel

	NTrees	MinNodeSize	MaxDepth	nCuts	KS-score for signal (background)	BDT Score
BP1	100	3%	2	20	0.169 (0.097)	0.1
BP2	30	4%	2	20	0.144 (0.553)	-0.04
BP3	95	3%	2	20	0.136 (0.363)	0.3
BP4	90	3%	2	20	0.148 (0.028)	0.3

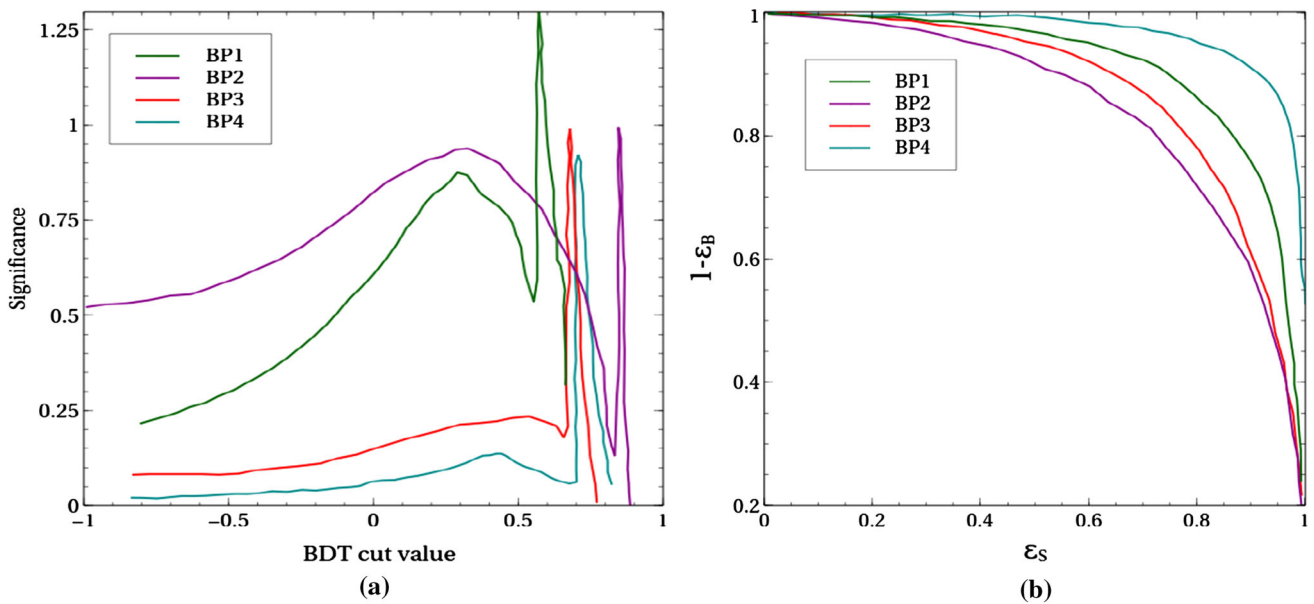


Fig. 12 (a) Variation of significance with BDT-score for $3l + 2b + \cancel{E}_T$ channel, (b) ROC curves for chosen benchmark points for $3l + 2b + \cancel{E}_T$ channel

ing) $|F|$ while keeping the significance fixed requires increasing (decreasing) $|A_{tb}|$ too. This is how the lower left corner of the $|F| - |A_{tb}|$ plane gets accessible, a region the $2b + 1l + 2j + \cancel{E}_T$ signal is blind to. For example, $|F| \simeq |A_{tb}| \simeq 0.1$ for $M_{H^+} = 200$ GeV prospects a 5σ -discovery potential. A complementarity between the two search channels is thus seen.

In order to see how the present analyses for a 27 TeV pp collider fares against the 14 TeV HL-LHC, we extrapolate the 13 TeV, 3 ab^{-1} analyses of the two VBF channels as reported in [57], to 14 TeV. The extrapolation procedure makes use of the fact that kinematical distributions, and hence, the cut-efficiencies do not change appreciably upon changing from $\sqrt{s} = 13$ TeV to 14 TeV. Keeping the integrated luminosity fixed, one can write $N_{S(B)}^{14} \simeq (\sigma_{S(B)}^{14}/\sigma_{S(B)}^{13})N_{S(B)}^{13}$ in that case, where $N_{S(B)}^{13}$ and $N_{S(B)}^{14}$ denote the number of signal (background) events at 13 TeV and 14 TeV respectively. The subscripts and superscripts of a cross section σ follow a similar notation. The contours in the $|F| - |A_{tb}|$ plane for 13 TeV can thus be extrapolated to 14 TeV (pink curve) as shown in Figs. 15 and 16. The 5σ discovery contours corresponding to the $2b + 1l + 2j + \cancel{E}_T$ channel are compared for 14 TeV and

27 TeV in Fig. 15. The 27 TeV collider at 15 ab^{-1} is seen to improve the sensitivity of the channel by a great margin. For example, the lowest value of $|A_{tb}|$ the HL-LHC can probe at 5σ is $\simeq 0.67$ and one requires a large $|F| = 1$ for it. The sensitivity for higher M_{H^+} is also seen to be much better for 27 TeV.

Figure 16 compares the 2σ exclusion contours corresponding to the $3l + 2j + \cancel{E}_T$ channel. For $M_{H^+} = 200$ and $|A_{tb}| = 0.1$, the HL-LHC demands $|F| \simeq 0.5$ for 2σ exclusion as opposed to the much lower $|F| \simeq 0.1$ in case of 27 TeV. The exclusion by a 27 TeV collider is seen to be much stronger than 14 TeV for the other masses also. In all, it is clearly established that a 27 TeV pp collider with 15 ab^{-1} integrated luminosity leads to a significant improvement of the VBF sensitivities.

The sensitivity we obtain in terms of the generic parameters $|F|$ and $|A_{tb}|$ can be straightforwardly translated to a realistic model containing singly charged boson(s) coupling dominantly to (t, b) and (W^\pm, Z) . As discussed before, a prime example is the Georgi-Machacek (GM) model [15] whose scalar sector comprises a real triplet ξ and a complex triplet Δ over and above the regular doublet. The triplets can

Table 22 The signal and background yields at 15 ab^{-1} for $M_{H^+} = 200 \text{ GeV}$, 300 GeV , 500 GeV and 1 TeV along with signal significances for the $3l + 2b + \cancel{E}_T$ channel after the BDTD analysis. The signal yields are computed for the $(F, \text{BR}(H^+ \rightarrow t\bar{b})) = (0.4, 0.4)$ reference point

$M_{H^+} = 200 \text{ GeV}$			$M_{H^+} = 300 \text{ GeV}$		
	Process	Yield at 15 ab^{-1}		Process	Yield at 15 ab^{-1}
Background	$t\bar{t}h$	5041	Background	$t\bar{t}h$	13,664
	$t\bar{t}Z$	15,490		$t\bar{t}Z$	44,515
	$t\bar{t}W$	855		$t\bar{t}W$	2020
	WZZ	51		WZZ	84
	ZZZ	15		ZZZ	22
	Zh	10		Zh	13
	Wh	3.5		Wh	5.8
	$b\bar{b}h$	0.045		$b\bar{b}h$	0.8
	Total	21,466		Total	60,325
Signal		146	Signal		335
Signal significance (0% $\sigma_{\text{sys_un}}$)		~ 1	Signal significance (0% $\sigma_{\text{sys_un}}$)		1.4
Signal significance (2% (5%) $\sigma_{\text{sys_un}}$)		0.32 (0.13)	Signal significance (2% (5%) $\sigma_{\text{sys_un}}$)		0.27 (0.11)
$M_{H^+} = 500 \text{ GeV}$			$M_{H^+} = 1 \text{ TeV}$		
	Process	Yield at 15 ab^{-1}		Process	Yield at 15 ab^{-1}
Background	$t\bar{t}h$	215	Background	$t\bar{t}h$	322
	$t\bar{t}Z$	4824		$t\bar{t}Z$	2582
	$t\bar{t}W$	59		$t\bar{t}W$	33
	WZZ	12		WZZ	7.8
	ZZZ	1.7		ZZZ	0.63
	Zh	0.26		Zh	0.05
	Wh	0.02		Wh	0.001
	$b\bar{b}h$	0.01		$b\bar{b}h$	0.004
	Total	5112		Total	2945
Signal		198	Signal		249
Signal significance (0% $\sigma_{\text{sys_un}}$)		2.8	Signal significance (0% $\sigma_{\text{sys_un}}$)		4.5
Signal significance (2% (5%) $\sigma_{\text{sys_un}}$)		1.6 (0.74)	Signal significance (2% (5%) $\sigma_{\text{sys_un}}$)		3.0 (1.5)

be expressed as,

$$\Delta = \begin{pmatrix} \frac{\delta^+}{\sqrt{2}} & \delta^{++} \\ \frac{v_\Delta + h_\Delta + iz_\Delta}{\sqrt{2}} & -\frac{\delta^+}{\sqrt{2}} \end{pmatrix},$$

$$\xi = \begin{pmatrix} \frac{v_\xi + h_\xi}{\sqrt{2}} & \xi^+ \\ \xi^- & -\frac{v_\xi + h_\xi}{\sqrt{2}} \end{pmatrix}, \quad (18a)$$

Here v_Δ (v_ξ) refers to the vacuum expectation value (VEV) of the triplet Δ (ξ). With v_d denoting the VEV of the scalar doublet, one has $\sqrt{v_d^2 + 2v_\Delta^2 + 4v_\xi^2} = 246 \text{ GeV}$. A custodial-symmetric scalar potential such as in the GM model demands $v_\xi = v_\Delta/\sqrt{2}$ in which case there is no constraint on v_Δ from the ρ -parameter.

Counting the singly charged boson coming from the scalar doublet, the total number of singly charged scalars in the GM model becomes three. The corresponding 3×3 mass matrix is diagonalised by the action of a mixing angle α giving rise

to a charged goldstone G^+ , and, the physical scalars H_3^+ and H_5^+ . Most importantly, both couple to W^\pm , Z and the third generation quarks for an arbitrary α . More precisely,

$$F = \frac{gv_\Delta}{c_W M_W} \sin\alpha, \quad A_{tb} = \frac{2v_\Delta}{v_d} V_{tb} \cos\alpha \quad \text{for } H_3^+, \quad (19a)$$

$$F = -\frac{gv_\Delta}{c_W M_W} \cos\alpha, \quad A_{tb} = \frac{2v_\Delta}{v_d} V_{tb} \sin\alpha \quad \text{for } H_5^+. \quad (19b)$$

c_W being the cosine of Weinberg angle.

That the $H^+ W^- Z$ interaction is proportional to the triplet VEV is a generic feature of models featuring scalar triplets. The sensitivity contours in the $|F|$ - $|A_{tb}|$ plane can therefore be mapped to the v_Δ - $|\sin\alpha|$ plane for the GM model for a given charged boson.

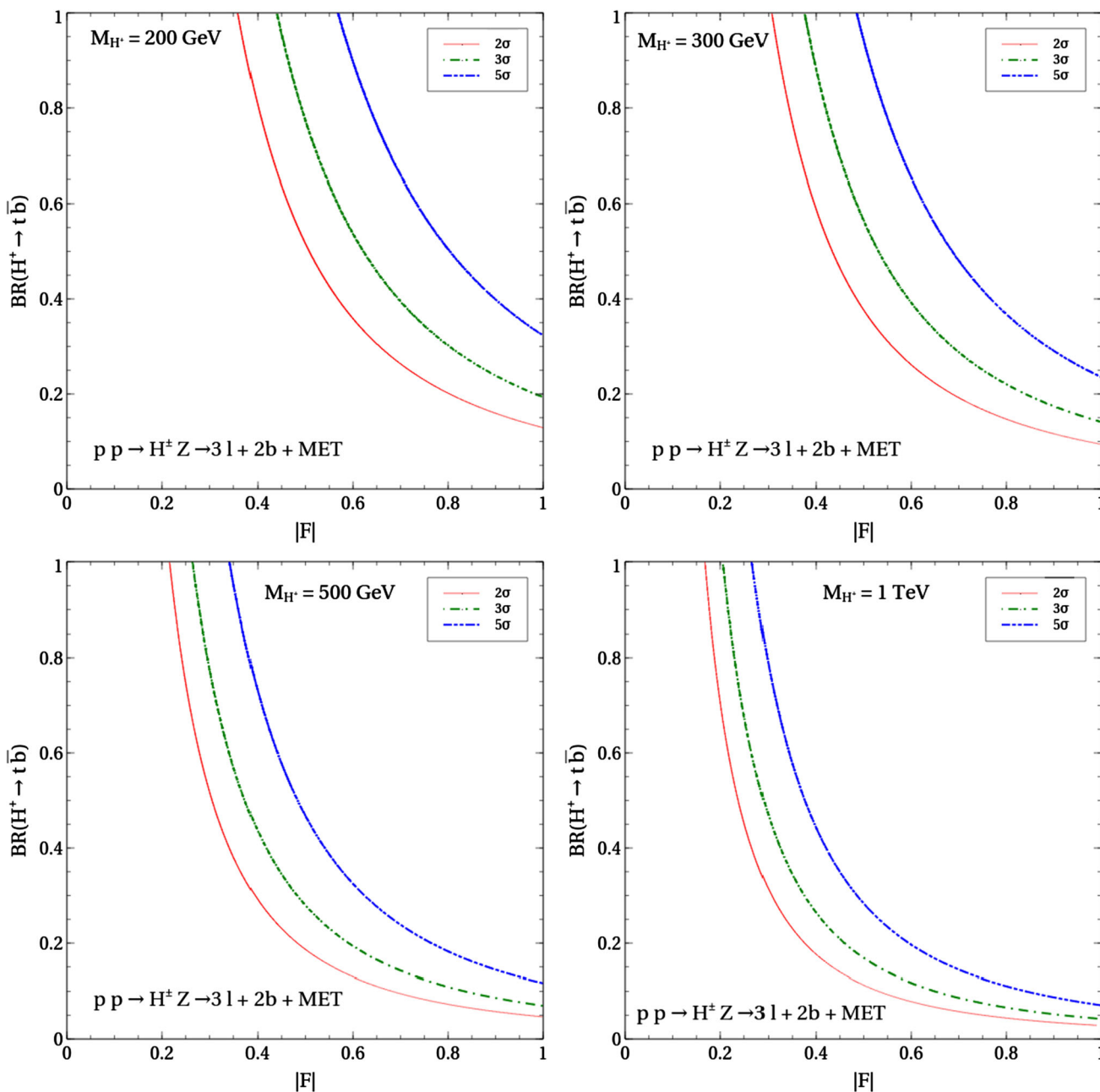


Fig. 13 The 2σ , 3σ and 5σ contours for the $pp \rightarrow ZH^\pm, H^+ \rightarrow t\bar{b}$ signal in the $|F|$ - $BR(H^+ \rightarrow t\bar{b})$ plane for different M_{H^\pm}

Figure 17 displays the contours for $H_5^{+\pm}$ ⁸ and the colour-coding remains the same as in Fig. 14.⁹ It is worthwhile here to comment on how the choice of α impacts the observability.

⁸ There exist other GM model parameters [25, 74] such as scalar couplings, masses and mixing angles that directly do not enter a parameter region shown in the $v_\Delta - |\sin\alpha|$ plane. It can therefore be inferred that the entire $v_\Delta - |\sin\alpha|$ plane gets allowed by electroweak precision measurements by a judicious choice of the other model parameters. Hence, the impact of electroweak precision constraints is not separately investigated for this mostly model-independent study.

⁹ We assume that H_3^+ is heavier than H_5^+ so that the $H_5^+ \rightarrow H_3^+ Z$ decay is disallowed kinematically.

The cross section of the $pp \rightarrow H_5^\pm jj, H_5^\pm \rightarrow t\bar{b}$ process is proportional to $\frac{F^2 A_{tb}^2}{F^2 + A_{tb}^2} = \left(\frac{4g^2 v_\Delta^4}{c_W^2 M_W^2 v_d^2} \right) \left\{ 1 / \left(\frac{g^2 v_\Delta^2}{c_W^2 M_W^2} c_\alpha^2 + \frac{4v_\Delta^2}{v_d^2} s_\alpha^2 \right) \right\} s_\alpha^2 c_\alpha^2$. Therefore, the cross section becomes maximum around maximal mixing, i.e. $\alpha = \frac{\pi}{4}$ thereby also maximising the observability. We find that a 27 TeV hadronic collider with an integrated luminosity of 15 ab^{-1} excludes an H_5^+ of mass 200 GeV at 95% confidence level for $v_\Delta \gtrsim 32$ GeV in the vicinity of maximal mixing, a significant improvement over an earlier 13 TeV study [63] that reports $v_\Delta \gtrsim 70$ GeV to be the corresponding exclusion limit. The discov-

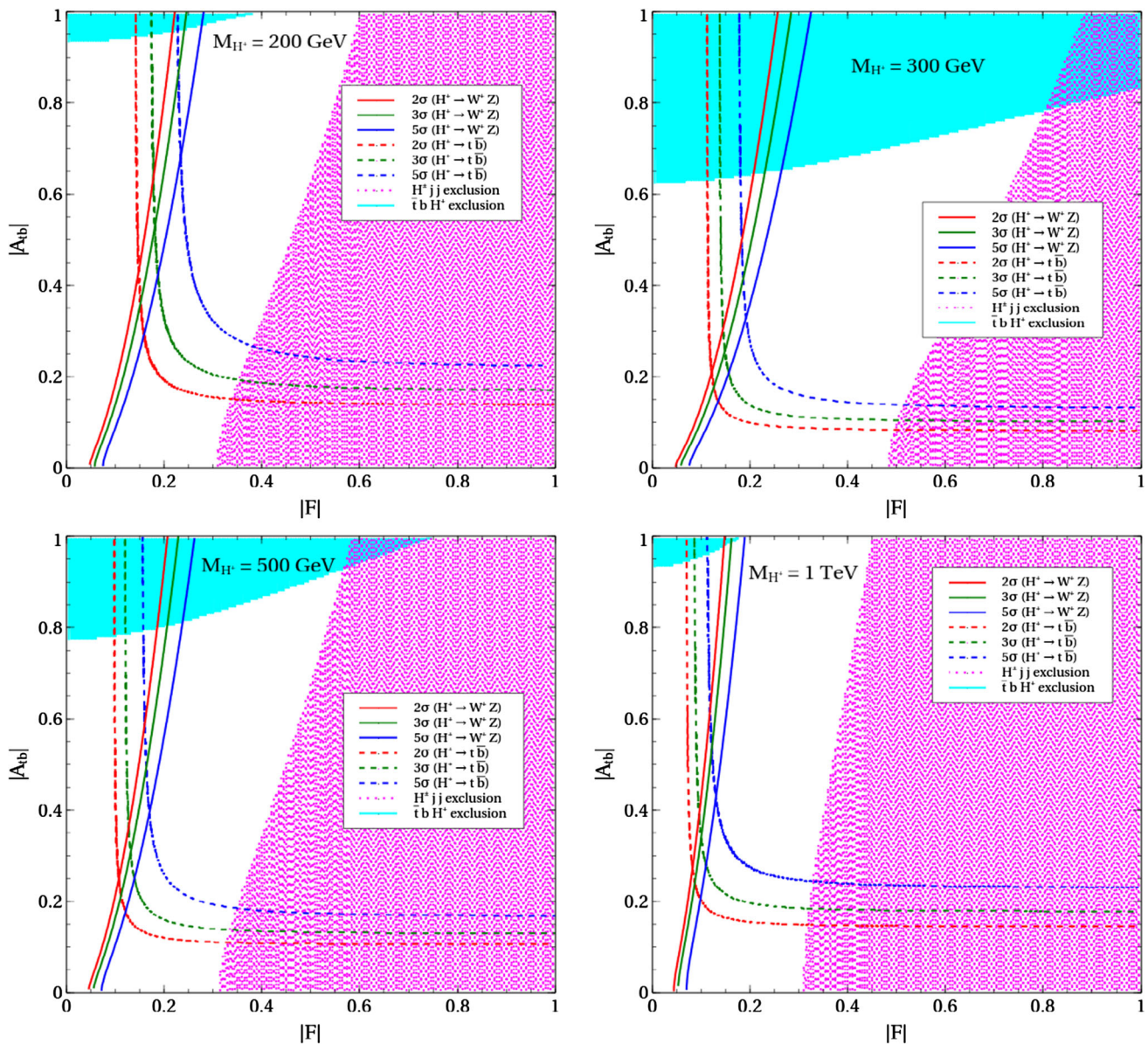


Fig. 14 $2\sigma, 3\sigma$ and 5σ contours in the $|F|$ - $|A_{tb}|$ plane for different M_{H^+} . The magenta (light blue) region is ruled out at 95% confidence level by the $pp \rightarrow H^\pm jj$, $H^\pm \rightarrow W^\pm Z$ ($pp \rightarrow tbH^\pm$, $H^\pm \rightarrow tb$) search

ery potential also markedly improves upon switching from 13 TeV to 27 TeV. We read from Fig. 17 that a maximally mixing H_5^+ of mass 200 GeV can be discovered at 5σ for $v_\Delta \gtrsim 48$ GeV. For $M_{H^+} = 300$ GeV, 500 GeV and 1 TeV, the minimum values of v_Δ leading to a 5σ observability are $\simeq 35$ GeV, 37 GeV and 39 GeV respectively. In complementarity with a discussion on maximal mixing, low values of $\sin\alpha$ can be probed taking high v_Δ . For example, taking $v_\Delta = 90$ GeV implies that the lowest $|\sin\alpha|$ allowing for a 5σ -discovery of an H_5^+ of mass equaling 200 GeV, 300 GeV, 500 GeV and 1 TeV are $\simeq 0.21$, 0.12, 0.15 and 0.20 respectively.

The lower left corner of the $|F| - |A_{tb}|$ plane that the $pp \rightarrow H_5^\pm jj$, $H_5^\pm \rightarrow W^\pm Z$ process can probe maps to the

low v_Δ -low $|\sin\alpha|$ region of the GM model. This is concurred by an inspection of Fig. 17. For $|\sin\alpha| = 0.2$, an H_5^+ of mass 200 GeV is excluded by the present analysis for $v_\Delta \gtrsim 6$ GeV. Considering the corresponding bound from the CMS analysis 13 TeV and 36 fb^{-1} stands at $v_\Delta \gtrsim 50$ GeV, we deem our analysis a considerable improvement over the former and demonstrative of the potential of a 27 TeV pp -collider. A 5σ -discovery is predicted for $v_\Delta \gtrsim 9$ GeV. The sensitivity of this channel for the higher masses remains approximately the same in this corner of the v_Δ - $|\sin\alpha|$ plane as can be read from Fig. 17.

Prior to closing this section, we add that the results we obtained in this study can be interpreted in context of any

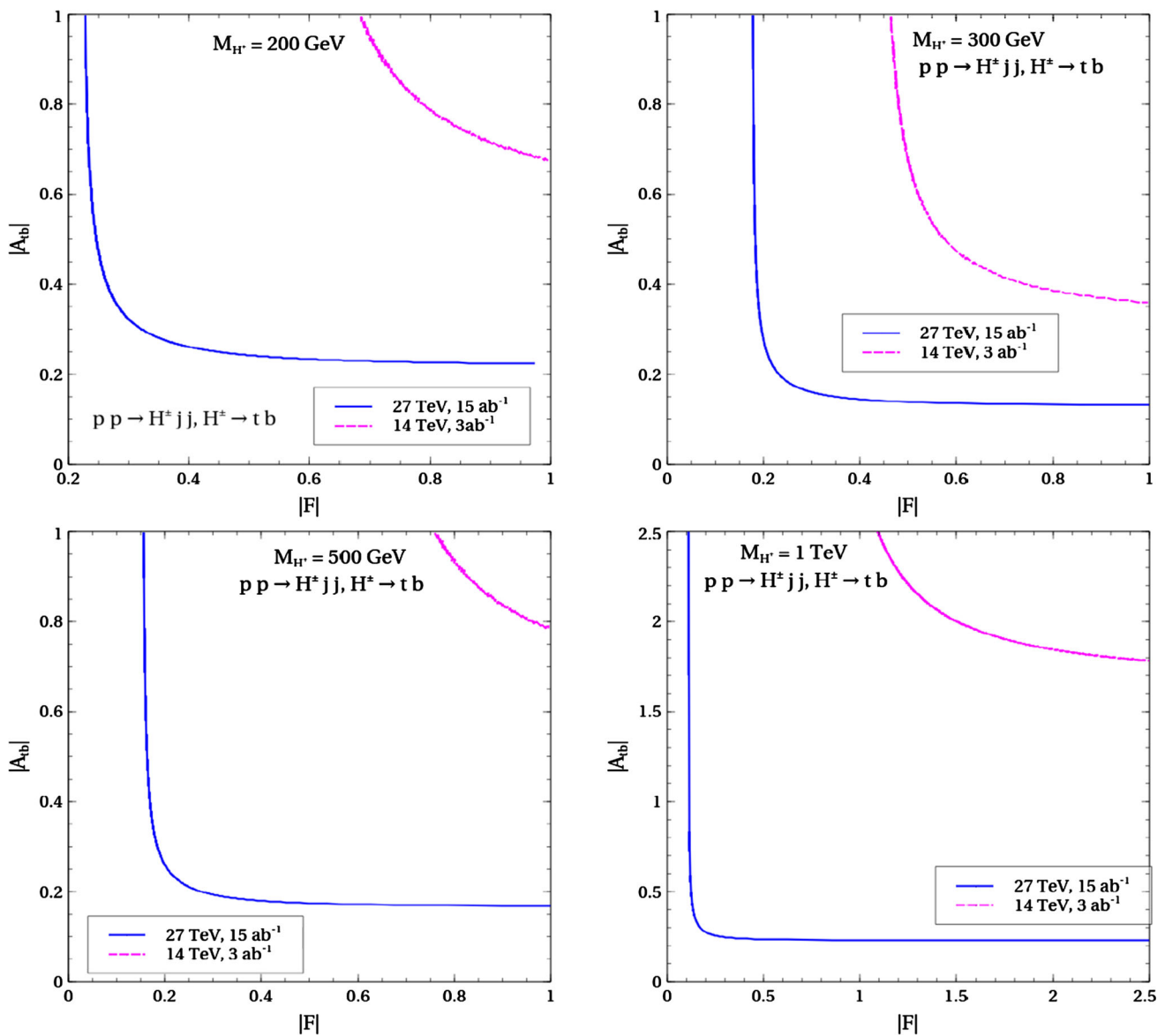


Fig. 15 The 5σ -discovery contours corresponding to the $2b + 1l + 2j + \cancel{E}_T$ channel in the $|F| - |A_{tb}|$ plane for the HL-LHC (magenta curve) and 27 TeV collider with 15 ab^{-1} integrated luminosity (blue curve)

NP scenario that predicts singly charged Higgs bosons dominantly coupling to the third generation quarks and W^\pm, Z . The non-minimal variants of the GM model can straightforwardly similarly be examined for observability of the singly charged scalars. However, we would like to comment on the observability in case of multi-doublet models where F is radiatively suppressed. As stated in the introduction, the Type-I 2HDM and its inert or color octet extensions predict $F \simeq \mathcal{O}(10^{-2})$ which is below the sensitivity threshold of the present analysis. That said, there is still the option of arbitrarily increasing the number of scalar doublets to enhance F and bring it within the sensitivity reach. However, such models are theoretically contorted and tightly constrained by experimental data. Overall, it can therefore be concluded

that despite such a huge enhancement in sensitivity compared to the HL-LHC, the 27 TeV pp machine with 15 ab^{-1} integrated luminosity cannot probe the radiative $H^+ W^- Z$ vertex, at least in the minimal multi-doublet models such as 2HDMs and 3HDMs.

6 Summary and conclusions

In this work, we have investigated the prospects of observing a gauge-phillic singly charged Higgs boson at the 27 TeV upgrade of the LHC attaining 15 ab^{-1} integrated luminosity. Motivated by certain realistic scenarios, it is assumed that the charged scalar dominantly interacts with (W^\pm, Z)

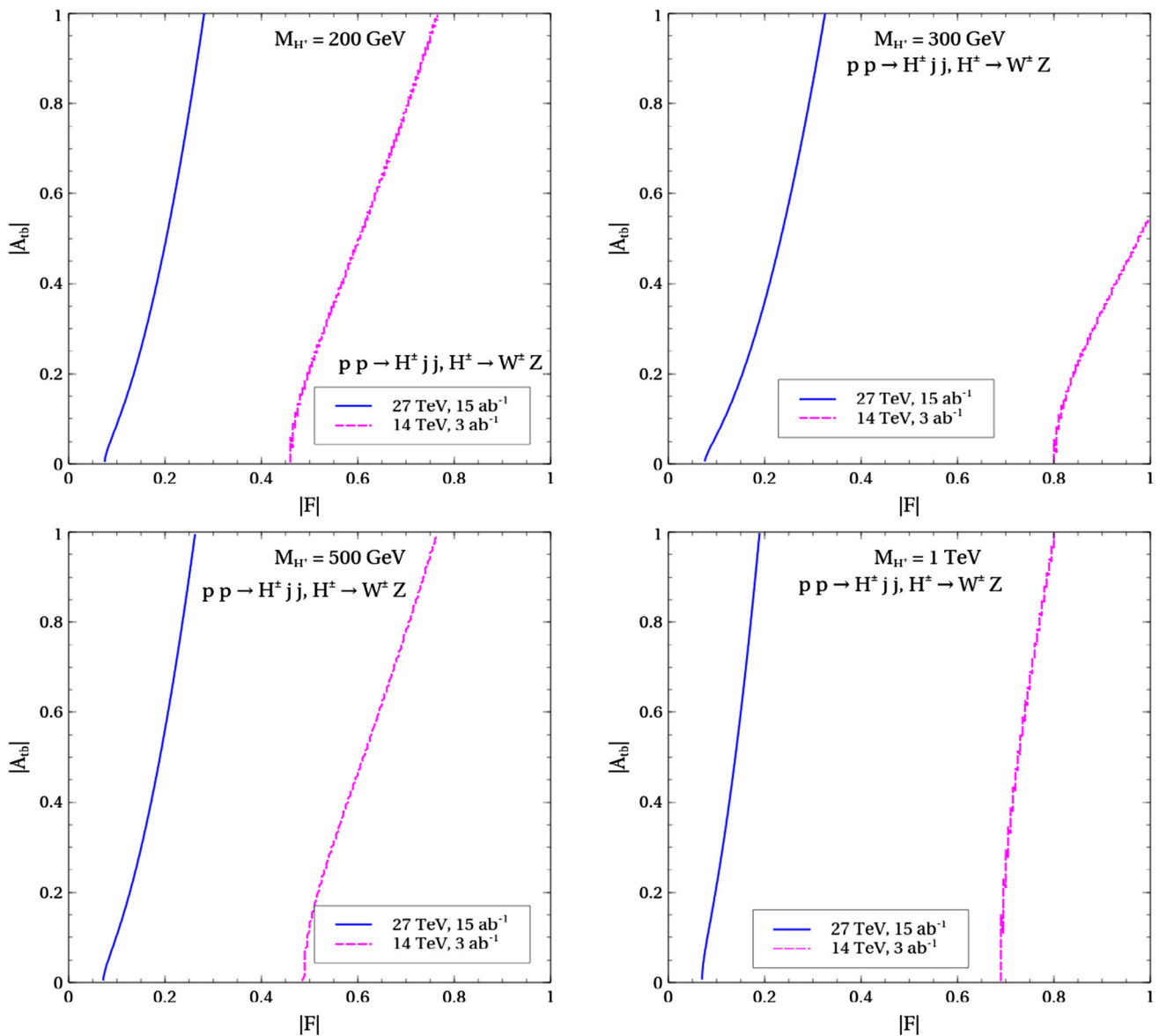


Fig. 16 The 2σ discovery contours corresponding to the $3l + 2j + \cancel{E}_T$ channel in the $|F| - |A_{tb}|$ plane for the HL-LHC (magenta curve) and 27 TeV collider with 15 ab^{-1} integrated luminosity (blue curve)

and (t, b) via the generic couplings F and A_{tb} respectively. Two kinematically distinct topologies for H^\pm production, i.e., the VBF process $pp \rightarrow H^\pm jj$ and $pp \rightarrow ZH^\pm$ are proposed for detailed study. The H^\pm so produced decays to the tb and $W^\pm Z$ pairs and complete leptonic cascades of the same are chosen for detailed analyses. That is, the following signals were analysed. (a) $pp \rightarrow H^\pm jj \rightarrow W^\pm Z jj \rightarrow 3l + 2j + \cancel{E}_T$, (b) $pp \rightarrow H^\pm jj \rightarrow tbjj \rightarrow 2b + 1l + 2j + \cancel{E}_T$, (c) $pp \rightarrow H^\pm Z \rightarrow W^\pm ZZ \rightarrow 5l + \cancel{E}_T$ and (d) $pp \rightarrow H^\pm Z \rightarrow tbZ \rightarrow 3l + 2b + \cancel{E}_T$, where $l = e, \mu$. We took $M_{H^\pm} = 200 \text{ GeV}, 300 \text{ GeV}, 500 \text{ GeV}$ and 1 TeV as benchmark mass points for the ensuing analysis. In addition to using the conventional cut-based method, multivariate tech-

niques stemming from the boosted-decision-tree algorithm were also adopted. We summarise below our key results.

- The statistical yield of the VBF production process supersedes that of the $pp \rightarrow ZH^\pm$ process for both $H^\pm \rightarrow W^\pm Z$ and $H^\pm \rightarrow tb$.
- The two VBF channels are seen to probe somewhat complementary regions of the $|F| - |A_{tb}|$ plane, which clearly is an upshot of the present analysis. The $pp \rightarrow H^\pm jj, H^\pm \rightarrow W^\pm Z$ signal is found to be able to probe the lower left corner of the $|F| - |A_{tb}|$ plane.
- The generic nature of the study has enabled to interpret the obtained results in context of the Georgi-Machacek

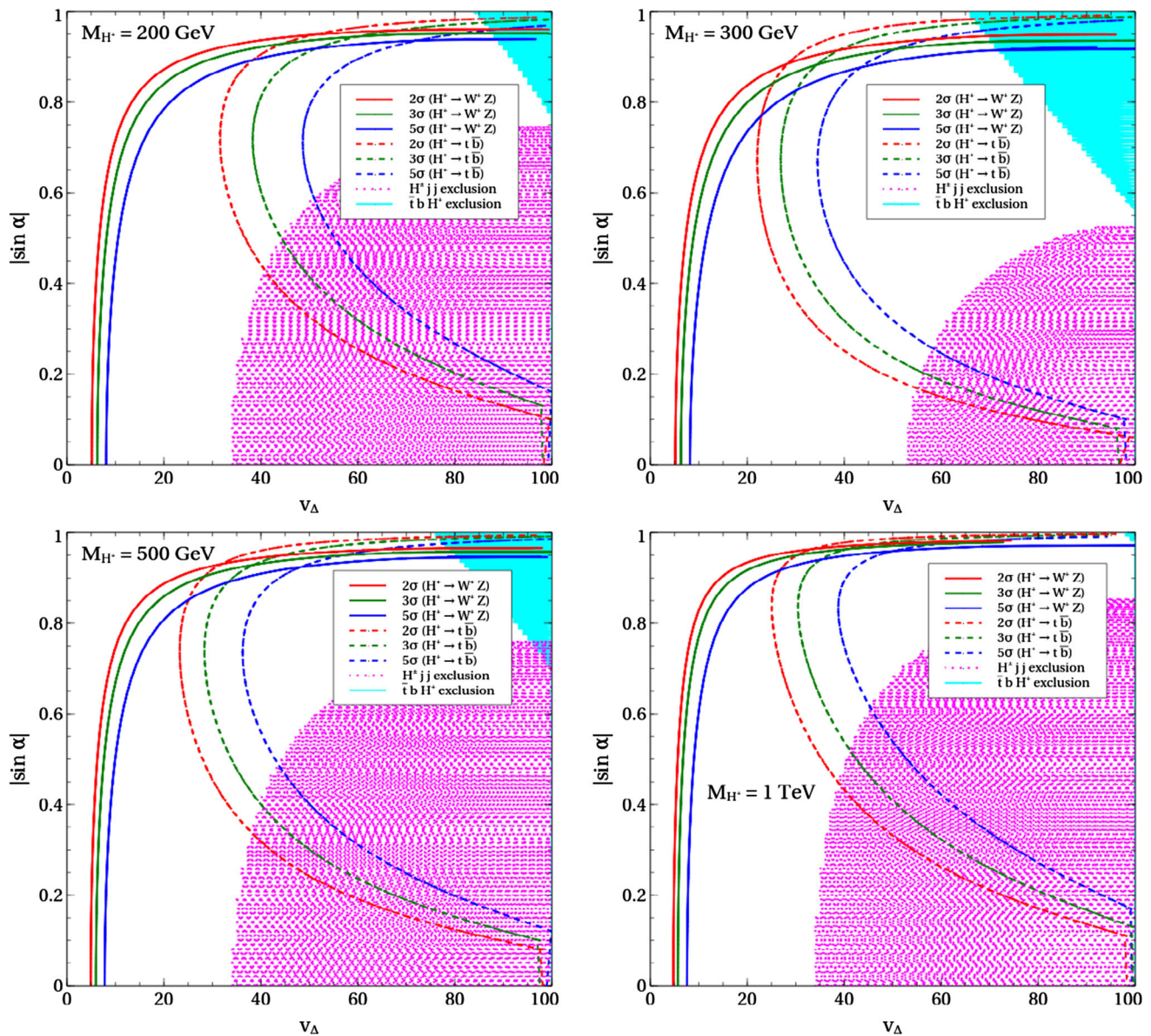


Fig. 17 $2\sigma, 3\sigma$ and 5σ contours in the v_Δ - $|\sin \alpha|$ plane for different M_{H^\pm} . The magenta (light blue) region is ruled out at 95% confidence level by the $pp \rightarrow H^\pm jj$, $H^\pm \rightarrow W^\pm Z$ ($pp \rightarrow t\bar{b} H^\pm$, $H^\pm \rightarrow t\bar{b}$) search

model. The relevant parameters for this case are the VEV v_Δ and the mixing angle α . The $pp \rightarrow H^\pm jj$, $H^\pm \rightarrow t\bar{b}$ signal predicts 5σ discovery of a 500 GeV charged scalar for a $v_\Delta \simeq 38$ GeV. With the $pp \rightarrow H^\pm jj$, $H^\pm \rightarrow W^\pm Z$, the 5σ threshold lowers to $v_\Delta \simeq 8$ GeV.

As a passing remark, our study highlights that the H^+W^-Z vertex is an important interaction to search for a singly charged Higgs boson. It also establishes that a $\sqrt{s} = 27$ TeV pp collider with an integrated luminosity of 15 ab^{-1} can be a powerful tool to improve the discovery potential of a charged Higgs via such an interaction over the earlier analyses carried out at lower centre-of-mass energies. The present

analysis therefore serves as an important case study on the efficacy of a 27 TeV hadronic collider.

Acknowledgements The authors sincerely thank Biplob Bhattacharjee for crucial inputs throughout the course of this work, and, for a careful reading of the manuscript. NC is financially supported by IISc (Indian Institute of Science) through the C.V.Raman postdoctoral fellowship. NC also acknowledges support from DST, India, under Grant Number IFA19-PH237 (INSPIRE Faculty Award). IC acknowledges support from DST, India, under Grant Number IFA18-PH214 (INSPIRE Faculty Award), and, hospitality extended by IISc while this work was in progress. The work of JL is supported by funding available from the Department of Atomic Energy, Government of India, for the Regional Centre for Accelerator-based Particle Physics (RECAPP), Harish-Chandra Research Institute.

Data Availability Statement This manuscript has no associated data or the data will not be deposited. [Authors' comment: The data we used in our manuscript to compare with our model estimations are already public from the ATLAS and CMS experiments.]

Open Access This article is licensed under a Creative Commons Attribution 4.0 International License, which permits use, sharing, adaptation, distribution and reproduction in any medium or format, as long as you give appropriate credit to the original author(s) and the source, provide a link to the Creative Commons licence, and indicate if changes were made. The images or other third party material in this article are included in the article's Creative Commons licence, unless indicated otherwise in a credit line to the material. If material is not included in the article's Creative Commons licence and your intended use is not permitted by statutory regulation or exceeds the permitted use, you will need to obtain permission directly from the copy-

right holder. To view a copy of this licence, visit <http://creativecommons.org/licenses/by/4.0/>.
Funded by SCOAP³.

Appendix A: Plots

We depict below the distribution of signal and backgrounds along with the KS-scores for each BP corresponding to the four channels (Figs. 18, 19, 20 and 21).

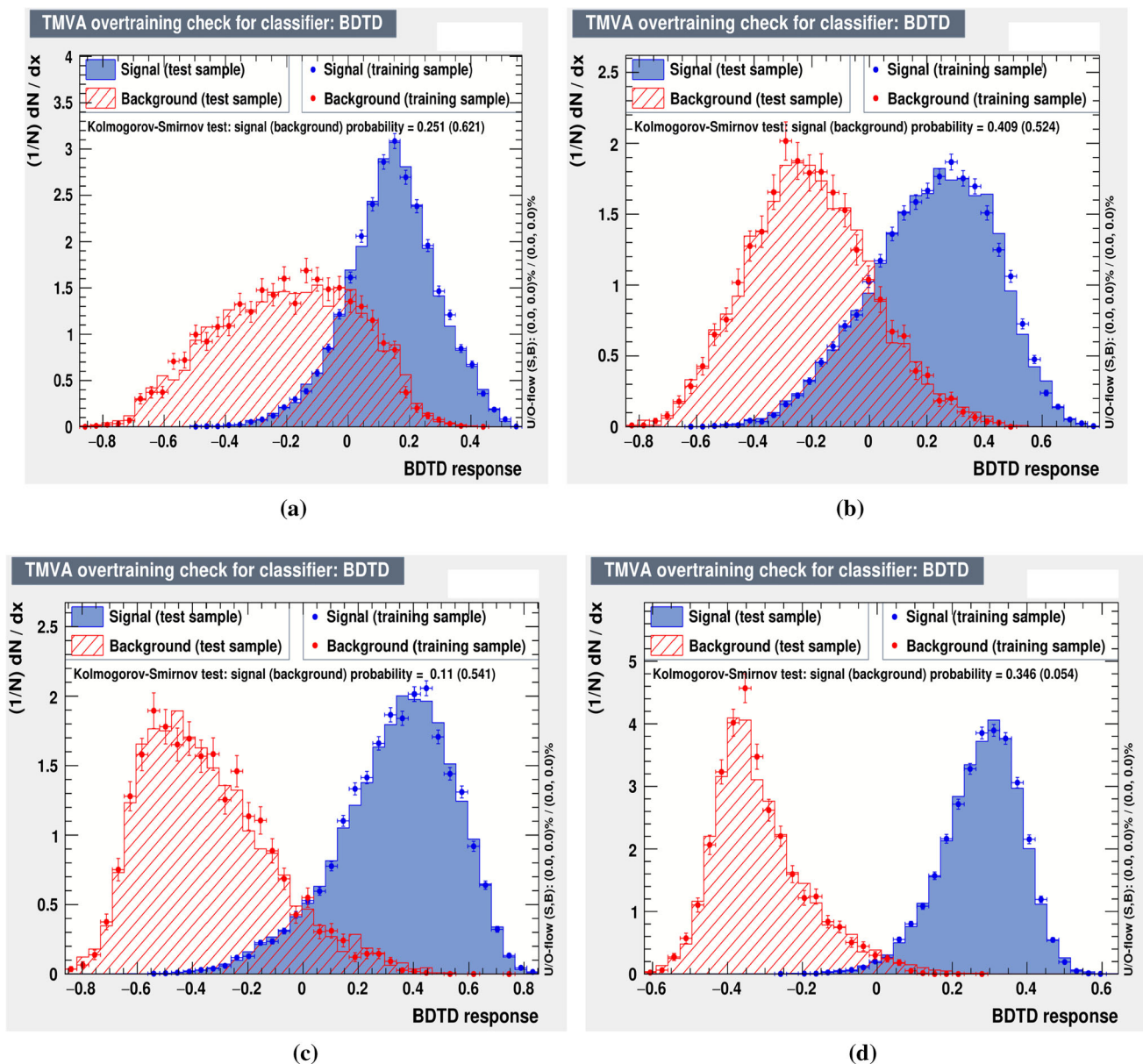


Fig. 18 KS-scores corresponding to BP1, BP2, BP3 and BP4 for $3l + 2j + \bar{E}_T$ channel

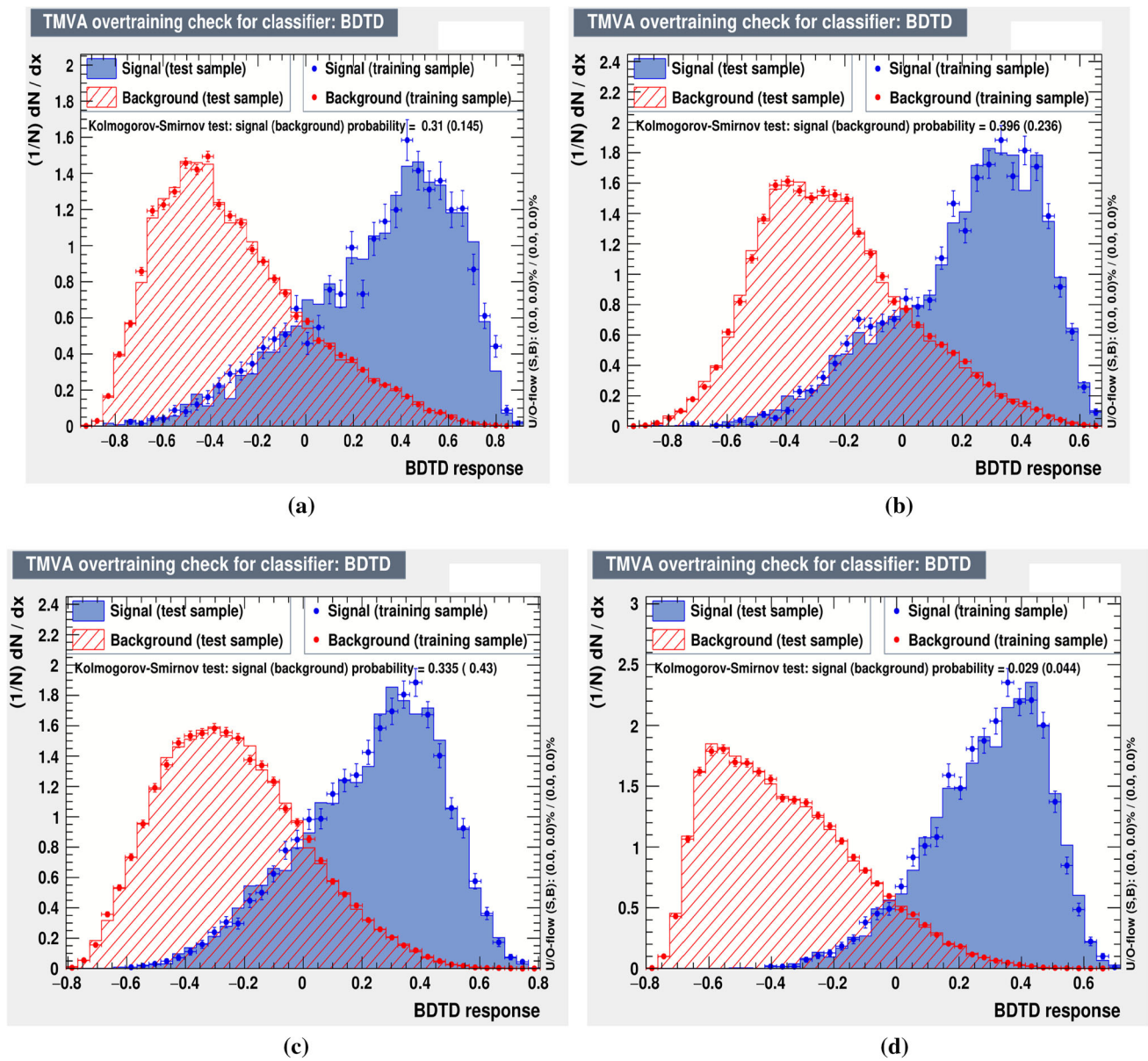


Fig. 19 KS-scores corresponding to BP1, BP2, BP3 and BP4 for $2b + 1l + 2j + \cancel{E}_T$ channel

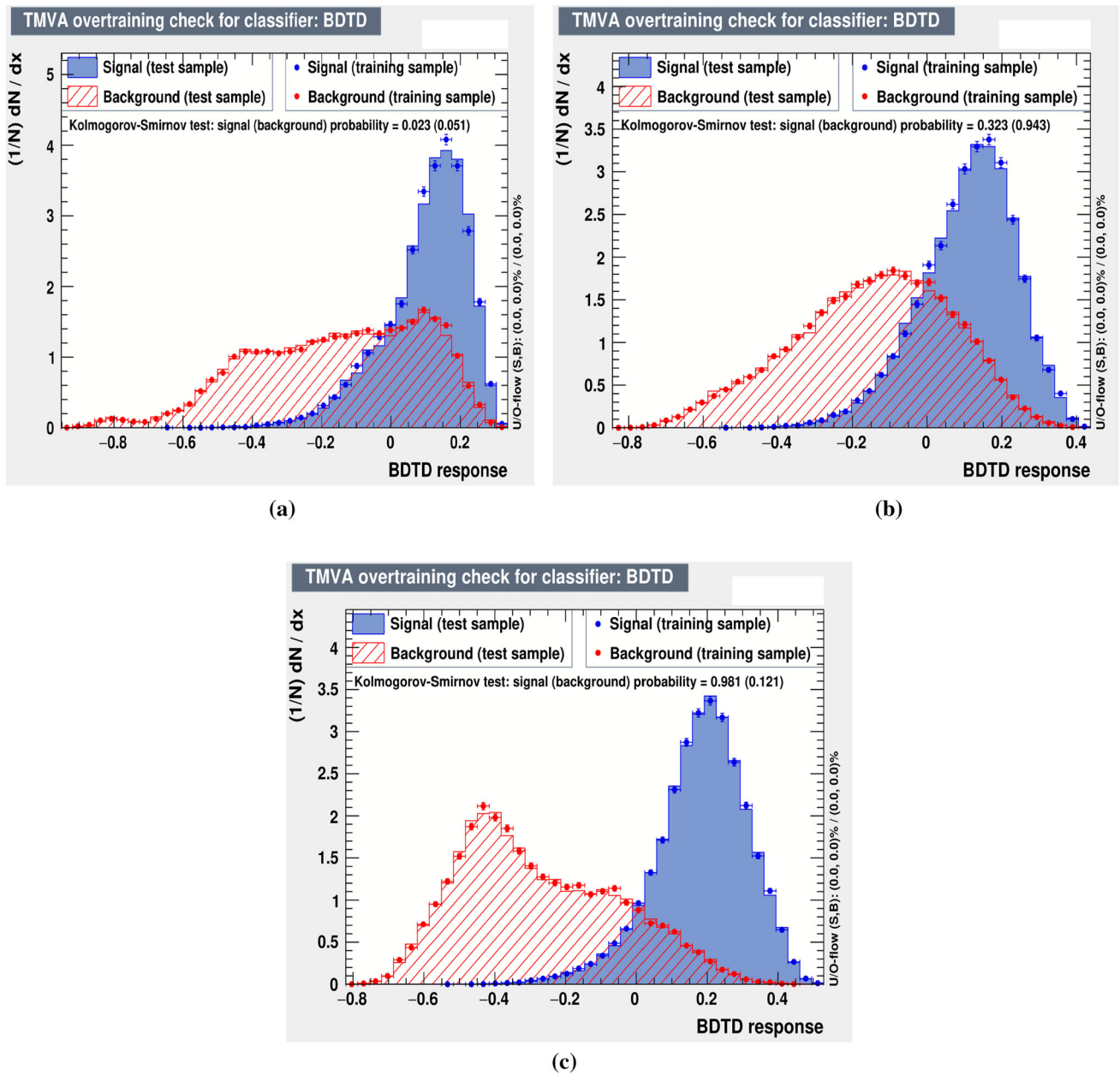


Fig. 20 KS-scores corresponding to BP1, BP2 and BP3 for $5l + \cancel{E}_T$ channel

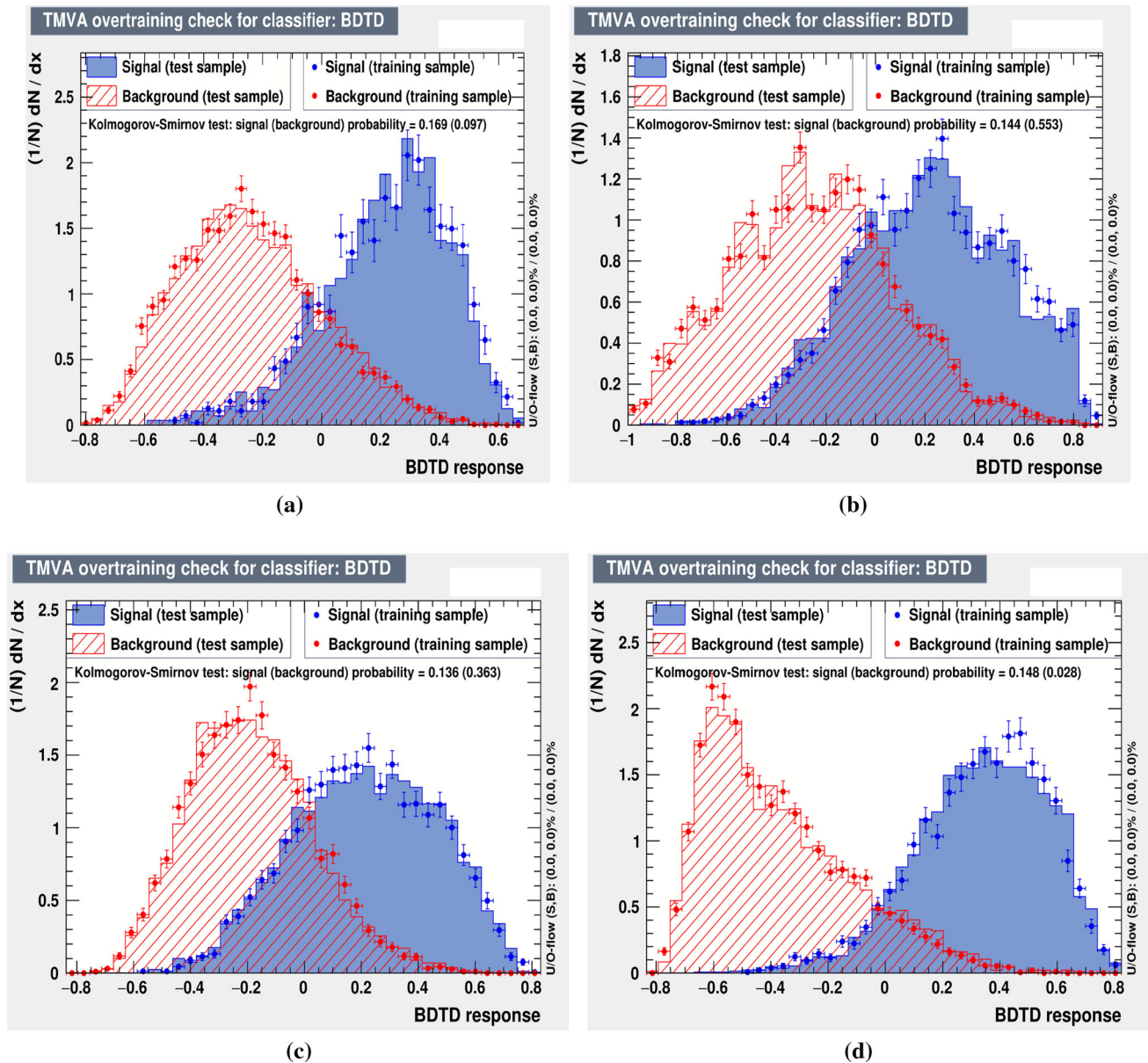


Fig. 21 KS-scores corresponding to BP1, BP2 and BP3 for $3l + 2b + \cancel{E}_T$ channel

References

1. G. Aad et al. (ATLAS), Phys. Lett. B **716**, 1 (2012). <https://doi.org/10.1016/j.physletb.2012.08.020>. arXiv:1207.7214 [hep-ex]
2. S. Chatrchyan et al. (CMS), Phys. Lett. B **716**, 30 (2012). <https://doi.org/10.1016/j.physletb.2012.08.021>. arXiv:1207.7235 [hep-ex]
3. N.G. Deshpande, E. Ma, Phys. Rev. D **18**, 2574 (1978). <https://doi.org/10.1103/PhysRevD.18.2574>
4. G.C. Branco, P.M. Ferreira, L. Lavoura, M.N. Rebelo, M. Sher, J.P. Silva, Phys. Rep. **516**, 1 (2012). <https://doi.org/10.1016/j.physrep.2012.02.002>. arXiv:1106.0034 [hep-ph]
5. J.A. Grifols, A. Méndez, Phys. Rev. D **22**, 1725 (1980). <https://doi.org/10.1103/PhysRevD.22.1725>
6. J.F. Gunion, H.E. Haber, G.L. Kane, S. Dawson, Front. Phys. **80**, 1 (2000)
7. S. Kanemura, Phys. Rev. D **61**, 095001 (2000a). <https://doi.org/10.1103/PhysRevD.61.095001>. arXiv:hep-ph/9710237
8. S. Kanemura, Eur. Phys. J. C **17**, 473 (2000b). <https://doi.org/10.1007/s100520000480>. arXiv:hep-ph/9911541
9. G. Abbas, D. Das, M. Patra, Phys. Rev. D **98**, 115013 (2018). <https://doi.org/10.1103/PhysRevD.98.115013>. arXiv:1806.11035 [hep-ph]
10. A. Arhrib, R. Benbrik, M. Chabab, W. T. Chang, T.-C. Yuan, *Supersymmetry at LHC: theoretical and experimental perspectives. Proceedings, CTP Symposium, Cairo, Egypt, March 11–14, 2007*. Int. J. Mod. Phys. A **22**, 6022 (2007). <https://doi.org/10.1142/S0217751X07039201>. arXiv:0708.1301 [hep-ph]
11. J. Schechter, J.W.F. Valle, Phys. Rev. D **22**, 2227 (1980). <https://doi.org/10.1103/PhysRevD.22.2227>
12. M. Magg, C. Wetterich, Phys. Lett. **94B**, 61 (1980). [https://doi.org/10.1016/0370-2693\(80\)90825-4](https://doi.org/10.1016/0370-2693(80)90825-4)

13. G. Lazarides, Q. Shafi, C. Wetterich, Nucl. Phys. B **181**, 287 (1981). [https://doi.org/10.1016/0550-3213\(81\)90354-0](https://doi.org/10.1016/0550-3213(81)90354-0)
14. T.P. Cheng, L.-F. Li, Phys. Rev. D **22**, 2860 (1980). <https://doi.org/10.1103/PhysRevD.22.2860>
15. H. Georgi, M. Machacek, Nucl. Phys. B **262**, 463 (1985). [https://doi.org/10.1016/0550-3213\(85\)90325-6](https://doi.org/10.1016/0550-3213(85)90325-6)
16. M.S. Chanowitz, M. Golden, Phys. Lett. **165B**, 105 (1985). [https://doi.org/10.1016/0370-2693\(85\)90700-2](https://doi.org/10.1016/0370-2693(85)90700-2)
17. J.F. Gunion, R. Vega, J. Wudka, Phys. Rev. D **42**, 1673 (1990). <https://doi.org/10.1103/PhysRevD.42.1673>
18. M. Aoki, S. Kanemura, Phys. Rev. D **77**, 095009 (2008). [Erratum: Phys. Rev. D **89**(5), 059902 (2014)]. <https://doi.org/10.1103/PhysRevD.89.059902>. <https://doi.org/10.1103/PhysRevD.77.095009>. arXiv:0712.4053 [hep-ph]
19. C.-W. Chiang, K. Yagyu, JHEP **01**, 026 (2013). [https://doi.org/10.1007/JHEP01\(2013\)026](https://doi.org/10.1007/JHEP01(2013)026). arXiv:1211.2658 [hep-ph]
20. K. Hartling, K. Kumar, H.E. Logan, Phys. Rev. D **90**, 015007 (2014). <https://doi.org/10.1103/PhysRevD.90.015007>. arXiv:1404.2640 [hep-ph]
21. K. Hartling, K. Kumar, H.E. Logan, Phys. Rev. D **91**, 015013 (2015). <https://doi.org/10.1103/PhysRevD.91.015013>. arXiv:1410.5538 [hep-ph]
22. C.-W. Chiang, S. Kanemura, K. Yagyu, Phys. Rev. D **90**, 115025 (2014). <https://doi.org/10.1103/PhysRevD.90.115025>. arXiv:1407.5053 [hep-ph]
23. S. Blasi, S. De Curtis, K. Yagyu, Phys. Rev. D **96**, 015001 (2017). <https://doi.org/10.1103/PhysRevD.96.015001>. arXiv:1704.08512 [hep-ph]
24. H.E. Logan, V. Rentala, Phys. Rev. D **92**, 075011 (2015). <https://doi.org/10.1103/PhysRevD.92.075011>. arXiv:1502.01275 [hep-ph]
25. B. Keeshan, H.E. Logan, T. Pilkington, Phys. Rev. D **102**, 015001 (2020). <https://doi.org/10.1103/PhysRevD.102.015001>. arXiv:1807.11511 [hep-ph]
26. N. Ghosh, S. Ghosh, I. Saha, Phys. Rev. D **101**, 015029 (2020). <https://doi.org/10.1103/PhysRevD.101.015029>. arXiv:1908.00396 [hep-ph]
27. A. Banerjee, G. Bhattacharyya, N. Kumar, Phys. Rev. D **99**, 035028 (2019). <https://doi.org/10.1103/PhysRevD.99.035028>. arXiv:1901.01725 [hep-ph]
28. D. Azevedo, P. Ferreira, H.E. Logan, R. Santos, JHEP **03**, 221 (2021). [https://doi.org/10.1007/JHEP03\(2021\)221](https://doi.org/10.1007/JHEP03(2021)221). arXiv:2012.07758 [hep-ph]
29. G. Moulataka, M.C. Peyranère, (2020). arXiv:2012.13947 [hep-ph]
30. A. Ismail, B. Keeshan, H.E. Logan, Y. Wu, Phys. Rev. D **103**, 095010 (2021). <https://doi.org/10.1103/PhysRevD.103.095010>. arXiv:2003.05536 [hep-ph]
31. R. Zhou, W. Cheng, X. Deng, L. Bian, Y. Wu, JHEP **01**, 216 (2019). [https://doi.org/10.1007/JHEP01\(2019\)216](https://doi.org/10.1007/JHEP01(2019)216). arXiv:1812.06217 [hep-ph]
32. H. Sun, X. Luo, W. Wei, T. Liu, Phys. Rev. D **96**, 095003 (2017). <https://doi.org/10.1103/PhysRevD.96.095003>. arXiv:1710.06284 [hep-ph]
33. C. Degrande, K. Hartling, H.E. Logan, Phys. Rev. D **96**, 075013 (2017). [Erratum: Phys. Rev. D **98**(1), 019901 (2018)]. <https://doi.org/10.1103/PhysRevD.96.075013>. <https://doi.org/10.1103/PhysRevD.98.019901>. arXiv:1708.08753 [hep-ph]
34. J. Chang, C.-R. Chen, C.-W. Chiang, JHEP **03**, 137 (2017). [https://doi.org/10.1007/JHEP03\(2017\)137](https://doi.org/10.1007/JHEP03(2017)137). arXiv:1701.06291 [hep-ph]
35. M. Aaboud et al. (ATLAS), JHEP **11**, 085 (2018). [https://doi.org/10.1007/JHEP11\(2018\)085](https://doi.org/10.1007/JHEP11(2018)085). arXiv:1808.03599 [hep-ex]
36. G. Aad et al. (ATLAS), JHEP **03**, 127 (2016). [https://doi.org/10.1007/JHEP03\(2016\)127](https://doi.org/10.1007/JHEP03(2016)127). arXiv:1512.03704 [hep-ex]
37. V. Khachatryan et al. (CMS), JHEP **11**, 018 (2015). [https://doi.org/10.1007/JHEP11\(2015\)018](https://doi.org/10.1007/JHEP11(2015)018). arXiv:1508.07774 [hep-ex]
38. M. Aaboud et al. (ATLAS), JHEP **09**, 139 (2018). [https://doi.org/10.1007/JHEP09\(2018\)139](https://doi.org/10.1007/JHEP09(2018)139). arXiv:1807.07915 [hep-ex]
39. G. Aad et al. (ATLAS), JHEP **03**, 088 (2015). [https://doi.org/10.1007/JHEP03\(2015\)088](https://doi.org/10.1007/JHEP03(2015)088). arXiv:1412.6663 [hep-ex]
40. A.M. Sirunyan et al. (CMS), JHEP **11**, 115 (2018). [https://doi.org/10.1007/JHEP11\(2018\)115](https://doi.org/10.1007/JHEP11(2018)115). arXiv:1808.06575 [hep-ex]
41. V. Khachatryan et al. (CMS), JHEP **12**, 178 (2015). [https://doi.org/10.1007/JHEP12\(2015\)178](https://doi.org/10.1007/JHEP12(2015)178). arXiv:1510.04252 [hep-ex]
42. R. Patrick, P. Sharma, A.G. Williams, Phys. Lett. B **780**, 603 (2018). <https://doi.org/10.1016/j.physletb.2018.03.033>. arXiv:1710.08086 [hep-ph]
43. R. Patrick, P. Sharma, A.G. Williams, Nucl. Phys. B **917**, 19 (2017). <https://doi.org/10.1016/j.nuclphysb.2017.01.031>. arXiv:1610.05917 [hep-ph]
44. J. Li, R. Patrick, P. Sharma, A.G. Williams, JHEP **11**, 164 (2016). [https://doi.org/10.1007/JHEP11\(2016\)164](https://doi.org/10.1007/JHEP11(2016)164). arXiv:1609.02645 [hep-ph]
45. S. Moretti, R. Santos, P. Sharma, Phys. Lett. B **760**, 697 (2016). <https://doi.org/10.1016/j.physletb.2016.07.055>. arXiv:1604.04965 [hep-ph]
46. B. Coleppa, F. Kling, S. Su, JHEP **12**, 148 (2014). [https://doi.org/10.1007/JHEP12\(2014\)148](https://doi.org/10.1007/JHEP12(2014)148). arXiv:1408.4119 [hep-ph]
47. B. Coleppa, A. Sarkar, S.K. Rai, Phys. Rev. D **101**, 055030 (2020). <https://doi.org/10.1103/PhysRevD.101.055030>. arXiv:1909.11992 [hep-ph]
48. A.M. Sirunyan et al. (CMS), Phys. Rev. Lett. **119**, 141802 (2017). <https://doi.org/10.1103/PhysRevLett.119.141802>. arXiv:1705.02942 [hep-ex]
49. G. Aad et al. (ATLAS), Phys. Rev. Lett. **114**, 231801 (2015). <https://doi.org/10.1103/PhysRevLett.114.231801>. arXiv:1503.04233 [hep-ex]
50. P. Bandyopadhyay, K. Huitu, A. Sabanci Kececi, JHEP **05**, 026 (2015a). [https://doi.org/10.1007/JHEP05\(2015\)026](https://doi.org/10.1007/JHEP05(2015)026). arXiv:1412.7359 [hep-ph]
51. P. Bandyopadhyay, C. Coriano, A. Costantini, JHEP **09**, 045 (2015b). [https://doi.org/10.1007/JHEP09\(2015\)045](https://doi.org/10.1007/JHEP09(2015)045). arXiv:1506.03634 [hep-ph]
52. P. Bandyopadhyay, C. Coriano, A. Costantini, Phys. Rev. D **94**, 055030 (2016). <https://doi.org/10.1103/PhysRevD.94.055030>. arXiv:1512.08651 [hep-ph]
53. P. Bandyopadhyay, A. Costantini, JHEP **01**, 067 (2018). [https://doi.org/10.1007/JHEP01\(2018\)067](https://doi.org/10.1007/JHEP01(2018)067). arXiv:1710.03110 [hep-ph]
54. A.G. Akeroyd et al., Eur. Phys. J. C **77**, 276 (2017). <https://doi.org/10.1140/epjc/s10052-017-4829-2>. arXiv:1607.01320 [hep-ph]
55. P. Azzi et al., CERN Yellow Rep. Monogr. **7**, 1 (2019). <https://doi.org/10.23731/CYRM-2019-007.1>. arXiv:1902.04070 [hep-ph]
56. V.D. Barger, J.L. Hewett, R.J.N. Phillips, Phys. Rev. D **41**, 3421 (1990). <https://doi.org/10.1103/PhysRevD.41.3421>
57. J.-Y. Cen, J.-H. Chen, X.-G. He, G. Li, J.-Y. Su, W. Wang, JHEP **01**, 148 (2019). [https://doi.org/10.1007/JHEP01\(2019\)148](https://doi.org/10.1007/JHEP01(2019)148). arXiv:1811.00910 [hep-ph]
58. J. Diaz-Cruz, J. Hernandez-Sanchez, J. Toscano, Phys. Lett. B **512**, 339 (2001). [https://doi.org/10.1016/S0370-2693\(01\)00703-1](https://doi.org/10.1016/S0370-2693(01)00703-1). arXiv:hep-ph/0106001
59. S. Moretti, D. Rojas, K. Yagyu, JHEP **08**, 116 (2015). [https://doi.org/10.1007/JHEP08\(2015\)116](https://doi.org/10.1007/JHEP08(2015)116). arXiv:1504.06432 [hep-ph]
60. N. Chakrabarty, I. Chakraborty, D.K. Ghosh, Eur. Phys. J. C **80**, 1120 (2020). <https://doi.org/10.1140/epjc/s10052-020-08676-3>. arXiv:2003.01105 [hep-ph]
61. D. Chowdhury, O. Eberhardt, JHEP **05**, 161 (2018). [https://doi.org/10.1007/JHEP05\(2018\)161](https://doi.org/10.1007/JHEP05(2018)161). arXiv:1711.02095 [hep-ph]
62. M. Tanabashi et al. (Particle Data Group), Phys. Rev. D **98**, 030001 (2018). <https://doi.org/10.1103/PhysRevD.98.030001>
63. C.-W. Chiang, G. Cottin, O. Eberhardt, Phys. Rev. D **99**, 015001 (2019). <https://doi.org/10.1103/PhysRevD.99.015001>. arXiv:1807.10660 [hep-ph]

64. B.P. Roe, H.-J. Yang, J. Zhu, Y. Liu, I. Stancu, G. McGregor, Nucl. Instrum. Methods A **543**, 577 (2005). <https://doi.org/10.1016/j.nima.2004.12.018>. [arXiv:physics/0408124](https://arxiv.org/abs/physics/0408124)
65. ATLAS-CONF-2020-039 (ATLAS), (2020)
66. J. Alwall, R. Frederix, S. Frixione, V. Hirschi, F. Maltoni, O. Mattelaer, H.S. Shao, T. Stelzer, P. Torrielli, M. Zaro, JHEP **07**, 079 (2014). [https://doi.org/10.1007/JHEP07\(2014\)079](https://doi.org/10.1007/JHEP07(2014)079). [arXiv:1405.0301](https://arxiv.org/abs/1405.0301) [hep-ph]
67. T. Sjöstrand, S. Ask, J.R. Christiansen, R. Corke, N. Desai, P. Ilten, S. Mrenna, S. Prestel, C.O. Rasmussen, P.Z. Skands, Comput. Phys. Commun. **191**, 159 (2015). <https://doi.org/10.1016/j.cpc.2015.01.024>. [arXiv:1410.3012](https://arxiv.org/abs/1410.3012) [hep-ph]
68. J. de Favereau, C. Delaere, P. Demin, A. Giammanco, V. Lemaître, A. Mertens, M. Selvaggi (DELPHES 3), JHEP **02**, 057 (2014). [https://doi.org/10.1007/JHEP02\(2014\)057](https://doi.org/10.1007/JHEP02(2014)057). [arXiv:1307.6346](https://arxiv.org/abs/1307.6346) [hep-ex]
69. A. Hoecker, P. Speckmayer, J. Stelzer, J. Therhaag, E. von Toerne, H. Voss, M. Backes, T. Carli, O. Cohen, A. Christov, D. Dannheim, K. Danielowski, S. Henrot-Versille, M. Jachowski, K. Kraszewski, A. Krasznahorkay, Jr., M. Kruk, Y. Mahalalel, R. Ospanov, X. Prudent, A. Robert, D. Schouten, F. Tegenfeldt, A. Voigt, K. Voss, M. Wolter, A. Zemla, arXiv Physics e-prints (2007). [arXiv:physics/0703039](https://arxiv.org/abs/physics/0703039)
70. G. Cowan, K. Cranmer, E. Gross, O. Vitells, Eur. Phys. J. C **71**, 1554 (2011). [Erratum: Eur. Phys. J. C **73**, 2501 (2013)]. <https://doi.org/10.1140/epjc/s10052-011-1554-0>. [arXiv:1007.1727](https://arxiv.org/abs/1007.1727) [physics.data-an]
71. D.R. Tovey, JHEP **04**, 034 (2008). <https://doi.org/10.1088/1126-6708/2008/04/034>. [arXiv:0802.2879](https://arxiv.org/abs/0802.2879) [hep-ph]
72. <https://twiki.cern.ch/twiki/bin/view/LHCPhysics/LHCHXSWG1HELHCXsecs>
73. A. Lazopoulos, T. McElmurry, K. Melnikov, F. Petriello, Phys. Lett. B **666**, 62 (2008). <https://doi.org/10.1016/j.physletb.2008.06.073>. [arXiv:0804.2220](https://arxiv.org/abs/0804.2220) [hep-ph]
74. J.-Y. Cen, J.-H. Chen, X.-G. He, J.-Y. Su, Int. J. Mod. Phys. A **33**, 1850152 (2018). <https://doi.org/10.1142/S0217751X1850152X>. [arXiv:1803.05254](https://arxiv.org/abs/1803.05254) [hep-ph]